Vilnius University
Faculty of Physics
Institute of Photonics and Nanotechnology

Dominykas Augulis

Graphene-Assisted GaN Membranes Formation

Master's final thesis

Photonics and Nanotechnology study programme

Student	Dominykas Augulis
Approved	2024-05-23
Academic supervisor	prof. dr. Tadas Malinauskas
Director of the Institute	prof. dr. Ramūnas Aleksiejūnas

Vilnius 2024

Contents

Introduction

Flexible electronics technology is already being utilized in industrial and medical devices by worldwide users. This new generation of electronics assists in monitoring the vital signs of premature babies and athlete's hydration. Another application of this technology is in robotics, where flexible sensors enable robots to mimic the touch of living organisms. However, whether intended for humans or robots, these devices present a significant chemical and engineering challenge. This is due to electronic components typically being delicate and rigid.

One of the earliest milestones in flexible electronics was achieved by the team led by *T. Someya* at the University of Tokyo. They reported the development of flexible electronics, covering an area of 65 cm^2, which could be used as robot skin. This material was composed of polyimide plastic layers [1]. While this engineering breakthrough is fascinating, certain applications require higher carrier mobilities and physical properties that do not degrade under harsh environmental conditions. Consequently, inorganic optoelectronics emerges as a superior alternative [2].

Using inorganics for flexible electronics presents numerous challenges associated with significant mechanical mismatch between bulk inorganic semiconductors and flexible substrates. One solution is to produce thin layers, as thinner films are more flexible, given that the critical bending radius is smaller for thin films than for bulk materials [3]. Various fabrication strategies for thin inorganic films include epitaxial lift-off techniques using a chemically etched sacrificial layer, optically induced separation between the epilayer and substrate [4], brute-force mechanical spalling using a metal stressor layer, and two-dimensional (2D) material-assisted layer transfer with a metal stressor [3]. These thin layers afterward can be transferred onto flexible substrates.

In this study, the 2D material-assisted lift-off of thin gallium nitride (GaN) layers was studied. The 2D material acted as an interlayer between the substrate and the growing GaN, restricting strong bonding formation and facilitating subsequent layer exfoliation. Moreover, high crystal quality material can be grown with remote and pin-hole-assisted regimes, where the substrate underneath the 2D material modulates the growing structures [5]. Previous research has demonstrated the benefit of this technique for vertically stacked full-color micro-LEDs [6]. Additionally, this approach holds promise for applications in robotics, as GaN and its alloys exhibit strongly pronounced piezoelectric properties [7], which are advantageous for creating long-lasting robotic skins for precise stress measurements.

Thus, the objective of this study was to exfoliate GaN layers from graphene, which would serve as a platform for the formation of flexible membranes composed of group III nitrides.

To achieve this goal, several tasks were planned:

- Transfer graphene onto the growth substrate using the common wet transfer method and a novel approach involving a laminator.
- Grow GaN on graphene via metal-organic vapor phase epitaxy (MOVPE).
- Deposit a Ni stressor onto the epitaxial GaN and evaluate the residual stress of the stressor.
- Exfoliate GaN layers from 2D material and analyze them.

1 Background

1.1 Materials

1.1.1 Gallium nitride

Since the synthesis of the first polycrystalline GaN material in 1932 [8], GaN technology has matured significantly. Nowadays, commercially available GaN-based optoelectronic components are poised to play an important role in general lighting and power electronics. Additionally, there is still an ongoing exploration of new applications and integration into emerging technologies.

Structure and Properties

GaN, like other group-III nitrides, is thermodynamically stable at room temperature and atmospheric pressure in a wurtzite structure. In this structure, atoms are arranged in two interpenetrating hexagonally closely packed lattices. Each Ga atom is surrounded by four N atoms at the corners of a tetrahedron, and vice versa. Consequently, GaN has two lattice constants: a = 3.189 Å and c = 5.185 Å in the unstrained case [9]. Deviation from these parameters typically indicates strains induced by structural defects. In the wurtzite crystal structure, GaN lacks inversion symmetry along the c-axis ([0001] direction), and two distinct orientations are distinguished. The [0001] +c orientation is referred to as the "Ga-face," and the [0001] –c plane is referred to as the "N-face" (see Figure 1).

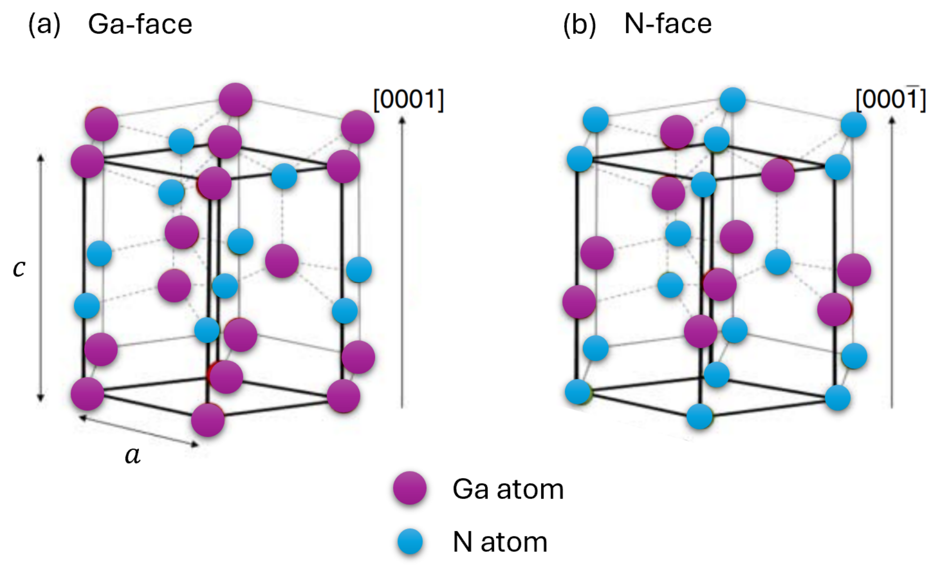
(a) Ga-face (b) N-face

Figure 1: Crystal structure of hexagonal (a) Ga-face and (b) N-face GaN. Solid lines represent the unit cell, and dashed lines depict bonds. Illustration adapted from literature [9].

These two orientations exhibit distinct chemical properties, resulting in different doping incorporation and afterward etching behaviors [9].

Furthermore, the GaN structure exhibits spontaneous polarization along the c-axis, attributed to the large electronegativity difference between Ga and N atoms and the lack of inversion symmetry for the GaN wurtzite crystal structure. The magnitude of this spontaneous polarization varies with the c_0/a_0 ratio of the lattice constant within the group III nitrides [9]. External stress can alter the c/a ratio, introducing an extra component to the polarization known as piezoelectric polarization. This property enables voltage induction in the active layers upon mechanical stress and can be exploited for sensing applications in skin-like electronics.

Nitrides are also popular for lighting applications due to their excellent optical properties. InN, GaN, and AlN possess direct band gaps corresponding to 0.7, 3.4, and 6.1 eV energies. A wide spectral range from infrared through the visible range to far ultraviolet can be achieved by forming ternary compounds from these materials. Also, functional structures such as quantum wells or quantum dots for optoelectronic purposes can be grown from nitrides using epitaxial methods, as described in the following paragraphs.

Proceeding, GaN and its alloys stand out as one of the best choices for power and high-frequency electronics. Being a wide-band gap material, GaN exhibits a high critical electric field, allowing the material to withstand high fields without breakdown. The electron mobility in GaN varies from 10^2 cm^2/Vs to almost 10^4 cm^2/Vs [10], depending on impurity concentration, doping, and temperature. In high electron mobility GaN/AlGaN/GaN structures, the mobility values typically ranges from 1100 to 2000 cm^2/Vs [9]. These mobility values enable device operation at higher frequencies compared to traditional GaAs technology.

Examining the electron velocity as a function of the electric field reveals a peak value close to 3×10^7, with the saturation velocity at about 1.5×10^7 [9]. These values indicate that GaN devices can operate at high frequencies and compete with GaAs and Si technology, as the mobility values for GaN are considerably higher.

The mentioned properties would differ if GaN crystallizes in a metastable zinc-blende structure when a cubic substrate is used or if a rock-salt structure is attained at elevated pressures [11].

Growth

Gallium nitride, being entirely man-made, is synthesized through various methods. The main growth techniques are sodium flux [12, 13], ammonothermal [12, 13], high-pressure nitrogen solution [12, 13], hydride vapor-phase epitaxy (HVPE) [12, 13], metalorganic vapor-phase epitaxy (MOVPE or MOCVD) [12], and molecular beam epitaxy (MBE) [14]. The materials produced using these techniques exhibit variations in maximal lateral size and defect concentration.

The first three methods are used for bulk crystal growth. HVPE, on the other hand, can be utilized for both thin film and bulk substrate growth. In contrast, MBE and MOVPE are preferred methods for achieving high crystalline quality thin films [12].

The key differences between MBE and MOVPE lie in growth temperatures and pressures, as well as in price, crystal quality, and the required cleanliness of rooms and equipment. Materials grown using MBE exhibit higher crystal quality, but the fabrication price is also higher, necessitating stringent clean-room conditions. Therefore, for commercial purposes, MOVPE reactors are more commonly employed.

In this study, a vertical MOVPE reactor from the AIXTRON brand, featuring a close-coupled shower head design, was employed to grow GaN. This reactor can be loaded with three 2-inch diameter wafers simultaneously and can be adjusted for usage with 4-inch diameter wafers.

The MOVPE reactor involves several key components, each playing a specific role in the growth mechanism. The main components of the MOVPE reactor used for GaN growth primarily consist of a reactor chamber, a high-temperature heating system, a cooling system, a gas-handling system, an exhaust system, and a control system (see Figure 2).

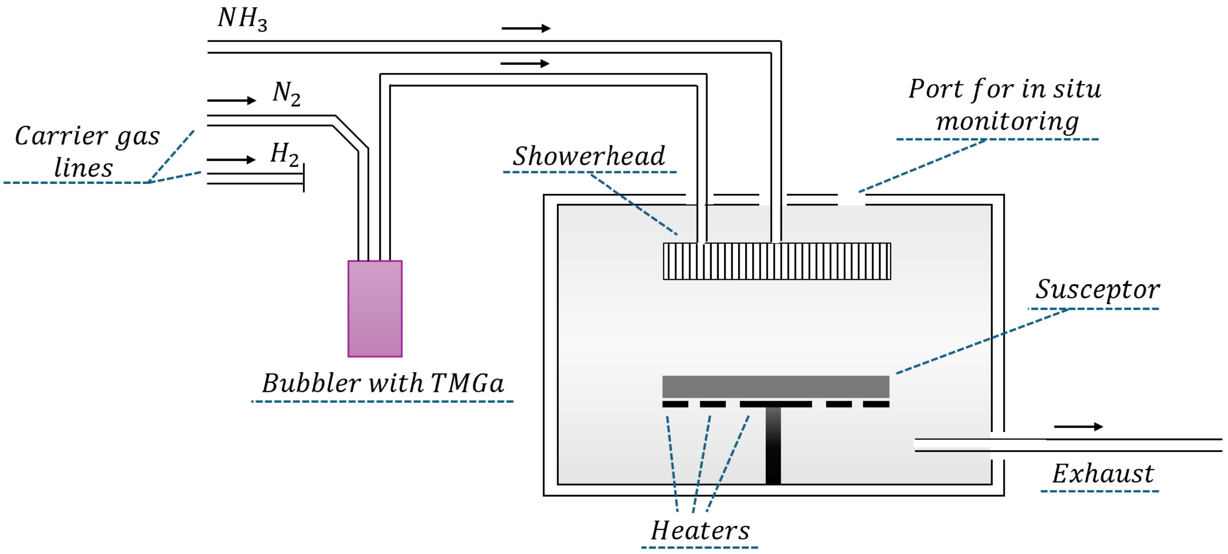

Figure 2: Representation of showerhead-type vertical MOVPE reactor configured for GaN growth. Illustration adapted from literature [15].

During the growth process, several gasses are employed. Ammonia (NH_3) plays a crucial role as a precursor for GaN growth, serving as the nitrogen source and reacting with metalorganic (MO) precursors to form GaN films. Trimethylgallium (TMGa) is one of the most common MO precursors for GaN growth [16]. MO is stored in a bubbler container. To transport and dilute TMGa, carrier gases such as N_2 or H_2 are utilized. The mixture of gases enters the reaction chamber through the shower head, and with a directional flux, they reach the substrates positioned on the susceptor surface.

The precursors decompose due to the high temperature of the susceptor, releasing the elements required for thin film growth. The main growth reactions occur on the substrate surface. By controlling the growth temperature and gas fluxes, thin films with different crystalline qualities can be grown. The growth can be monitored through *in situ* monitoring port. By-products of the gases used in the process are evacuated through the exhaust system.

For epitaxial GaN growth, various substrates can be chosen. Regarding quality, bulk GaN substrates are the optimal choice due to their perfect lattice match [17]. The details of epitaxial growth and the importance of lattice matching are further explained in Section 1.2. However, these bulk substrates often come with a relatively high cost, typically around 1000 €, depending on the wafer size and quality. Such elevated wafer prices are impractical for most commercial applications, leading to the consideration of more economical alternatives.

Cheaper alternatives such as $LiGaO_2$, GaAs, Si, SiC, and Al_2O_3 (sapphire) are often used [17].

These substrates have lattice constant mismatches with the growing GaN (GaN epilayer), resulting in high dislocation density (in the case of sapphire, around $10^{10} cm^{-2}$) [17]. On the other hand, manufacturing costs are significantly reduced. Moreover, the use of thin van der Waals materials (vdW) as an interlayer between the substrate and epilayer can reduce structural flaws resulting from growth on foreign substrates (see subsection 1.2.1). This study chose sapphire as the initial substrate, and GaN/sapphire templates were grown using well-established GaN growth technology. Subsequently, GaN was grown via a graphene interlayer.

1.1.2 Graphene

Structure and Properties

Since the practical discovery of graphene in 2004, it has become one of the most studied 2D materials in the world [18]. Graphene can be described as a 2D version of graphite and is widely researched because of its properties. In the 2D plane, carbon atoms are arranged in a hexagonal pattern. Graphene is one atom thick in the third dimension, with no free dangling bonds. The structure's thickness in the literature ranges from 0.4 to 1.7 nm, which differs from the inter-plane spacing of graphite, which is only 0.335 nm [19]. The primitive unit cell of graphene consists of two sp^2 hybridized carbon atoms (Figure 3(a)).

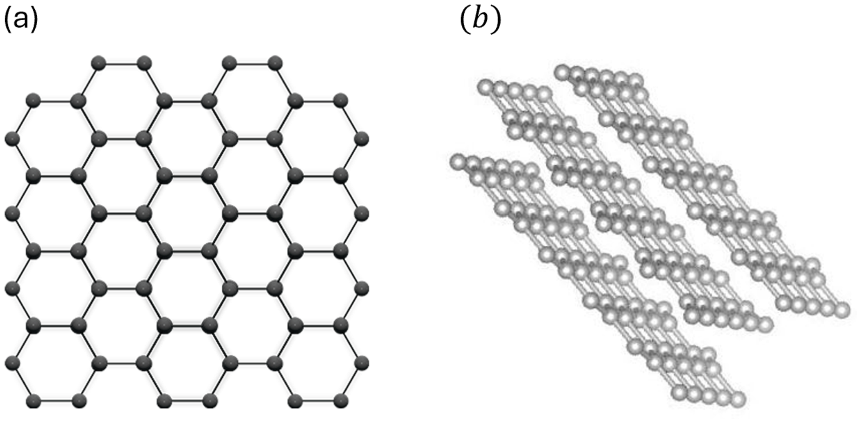

Figure 3: Structure of single layer and tri-layer graphene.

Such a single layer structure exhibits unique properties, such as high electron mobility reaching 10000 cm^2/Vs [20] and thermal conductivity of 3000 – 5000 Wm/K [18]. Graphene is an extremely thin material with an optical transparency of 97.4 %. However, its thinness does not restrict mechanical strength, with Young's modulus of 1 TPa [18].

Although graphene typically refers to a single-layer sheet of carbon atoms, a stack of a few carbon layers is also commonly called graphene. Figure 3(b) illustrates a tri-layer graphene stack. In a stacked structure, the vdW forces dominate between the layers. Its number of layers can modify the properties of graphene. For example, single-layer and bi-layer graphene have zero band gaps. However, an electric field can open a band gap in bi-layer graphene. Hence, it is crucial first to evaluate the number of graphene layers to understand its properties.

This work exploits the physical coupling properties between graphene and three-dimensional (3D) layers. These coupling effects arise from ionic-vdW and covalent-vdW interactions. They can be divided into several categories: electrical coupling, all-optical coupling, thermal coupling, lattice/strain decoupling, and vdW coupling [21]. The latter two can be utilized in the growth process of group III nitrides. The benefits of strain decoupling are important for thin films grown on vdW surfaces, enabling strain relaxation during epitaxy and extreme flexibility without affecting their physical characteristics. Additionally, vdW coupling permits the mechanical exfoliation of grown layers. Furthermore, the growth process on graphene can be influenced by the substrate underneath [3, 15, 22–24]. This is because graphene, being a two-dimensional material, is transparent to the atomic bonding potential, thereby allowing the transmission of the substrate's atomic bonding potential [21]. These effects will be further analyzed in the section 1.2.1.

Synthesis

Historically, the first layers of graphene were obtained using the *Scotch Tape* method. This method relies on micro-mechanical cleavage using adhesive tape, where bulk graphite is reduced into thinner flakes, eventually yielding 2D graphene. However, this approach has drawbacks: its yields are low, the quality is unsatisfactory, and the process is time-consuming. Consequently, alternative methods have been proposed [25].

Another method involves the chemical oxidation of graphite and its subsequent reduction into its 2D form. One of the newer methods involves unzipping carbon nanotubes, which are cylindrically rolled sheets of graphene. By unzipping them, graphene nanoribbons with precise dimensions can be created. However, graphene nanoribbons have a small surface area, which can be a drawback for some applications. A larger area of graphene can be created through the thermal decomposition of silicon carbide. In this technique, a silicon carbide sample is heated, causing silicon atoms to desorb from the sample's surface, leaving behind only carbon atoms forming graphene. This process occurs because the silicon saturated vapor pressure exceeds carbon's. An alternative large-scale technique is chemical vapor deposition (CVD). During CVD graphene growth, precursor gasses travel through a hot zone of a reactor. When gas species reach a metal substrate acting as a catalyst, hydrocarbon precursors break into carbon radicals. These radicals then self-assemble to form graphene. Several metal substrates and gas precursors can be selected for growth, and the selection will influence the quality of the grown layer. Common transitional metals used for growth substrates include Ru, Ir, Pt, Co, Pd, Ni, and Cu. In this work, the graphene used was synthesized on Cu. Such a process is usually conducted using methane on polycrystalline (111)- oriented Cu at higher than 1000 °C temperatures. Raman spectroscopy is commonly used for quality inspection to determine if the synthesis is successful.

High-quality graphene can be used in various applications, such as transistors, transparent displays, coatings, healthcare, medicine, batteries, and supercapacitors. In this study, however, the material was only used as an interlayer during the growth of GaN because of the mentioned properties.

1.2 Epitaxy

In this work, epitaxial growth of GaN is conducted, highlighting the need for a fundamental understanding of epitaxy. Epitaxy is a technique in which an epilayer attempts to align with the crystallographic orientation of a crystalline substrate. This process can be further classified into subcategories based on nucleation and growth regimes. The most commonly utilized method is conventional epitaxy, where nucleation and growth on the substrate occur through the formation of covalent or ionic bonds at the interface. Bond formation relies heavily on growth conditions and the selection of substrates and epilayer materials with relatively matching properties.

If the substrate is the same material as the film to be grown, the method is referred to as homoepitaxy. In this regime, the epitaxial film's dislocation density and interfacial defects are nearly non-existent, allowing for the growth of high-quality epilayers. However, the substrate selection is rather limited, and the grown layers are tightly bonded to a non-flexible bulk substrate without a clear identification of where the epilayer begins.

Furthermore, modern devices typically necessitate heterojunctions, which require the integration of different material layers. Conventional heteroepitaxy is commonly employed to achieve high-quality crystalline materials in heterojunctions. However, achieving perfect matching conditions between the substrate and the epilayer's crystal structure and thermal expansion coefficients is often impossible. Consequently, there is always an accumulation of defects, such as threading dislocations, which can introduce undesirable physical properties [26, 27]. This problem is accompanied by the challenges encountered in homoepitaxy, where the epilayer is tightly bonded to the substrate.

Alternatively, other epitaxial growth techniques exist, such as nanoepitaxy, used for the growth of small-scale structures like quantum dots or nanowires, and 2D-material-assisted epitaxy, which has the potential to overcome many of the challenges associated with both conventional hetero and homoepitaxy [5, 26].

Epitaxial growth regimes can be achieved using physical or chemical vapor deposition methods [26]. In this study, MOVPE was utilized for conventional heteroepitaxy and 2D-material-assisted epitaxy of GaN growth.

1.2.1 Van der Waals, remote and pinhole-based epitaxy

Three distinct epitaxy mechanisms can come into play when a 2D material or nearly 2D material (up to a few layers) without dangling bonds is implemented as an interlayer between the substrate and the material to be grown. These regimes are defined as remote, vdW, and pinhole-based epitaxy methods (see Figure 4) [5, 26, 27]. In this work, 2D material is synonymous with a material of one atom thickness.

The interchange between these methods can vary depending on the quality of the 2D material (structural defects), its thickness, and the polarity (or ionicity) of both the substrate and the 2D material [5]. When the atomically thin interlayer is structurally perfect and without dangling bonds, two regimes based on the 2D material and substrate ionicity emerge.

In cases where a substrate possesses high ionicity/polarity, it can pass through a lattice-transparent

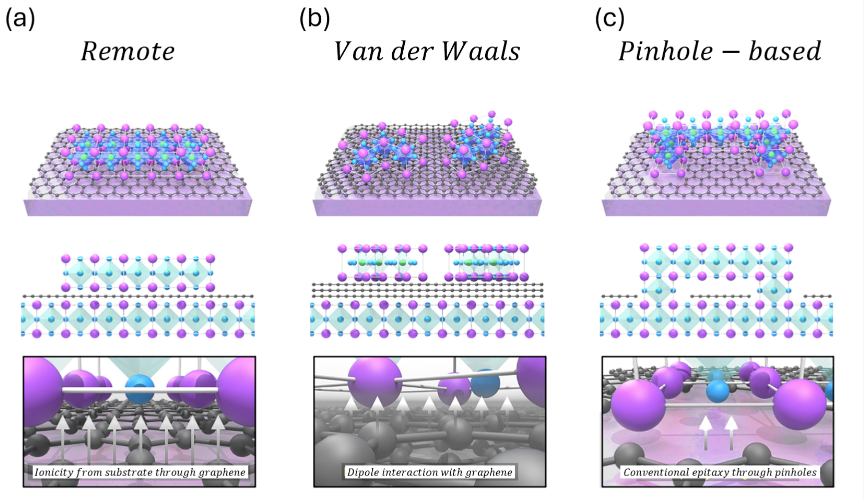

Figure 4: 2D material-assisted epitaxy regimes: (a) remote, (b) vdW, and (c) pinhole-based. In the illustration, graphene is depicted as the interlayer material. The middle part of the image with cross-sectional views summarizes the bond formation. There is no bonding (only weak vdW interaction) between the interlayer, substrate, and epilayer. However, nucleation and bonding differ based on the regime. The illustration is adapted from literature [5].

.

ultrathin 2D vdW interlayer such as a graphene monolayer, resulting in a remote epitaxy. In this regime, the force attracting adatoms is determined by the partially penetrated bonding potential of the substrate. Consequently, the epilayer mimics the underlying substrate, promoting nucleation and epitaxial growth aligned with it. This method surpasses conventional epitaxy as no chemical bonds are formed at the interface, reducing strains arising from a lattice mismatch and allowing high-quality material growth. Furthermore, such epilayers can easily exfoliate with stressors, resulting in relatively smooth surfaces [5].

The remote regime vanishes as the vdW interlayer thickens or the substrate has lower ionicity. This happens because the substrate's electrostatic potential cannot penetrate the interlayer, and epitaxy based on vdW interaction emerges. In the vdW regime, the adatoms of the epilayer are arranged in the lattice pattern of the 2D material without forming chemical bonds. Epilayer lattice alignments do not adapt to the underlying substrate. This regime allows the growth of materials with high lattice mismatches that can be easily exfoliated. However, a drawback of this process is the quality of the epilayer, as the lack of electrostatic potential from the underlying substrate prevents the establishment of specific crystalline orientations during growth. Therefore, polycrystalline layers are commonly obtained.

A different regime appears in the case of an interlayer with pinholes. In this method, nucleation happens through pinholes in the 2D layer. Thus, epitaxial layers are formed due to lateral overgrowth over the 2D interlayer. Thus, chemical bonds are formed with a substrate similar to conventional epitaxy. The positioning of adatoms is mainly governed by the substrate rather than the 2D layer. Local strain from lattice mismatch forms in the pinhole sides. Layers grown with pinhole-based epitaxy can be exfoliated. However, it may lead to fracture damage of the substrate.

In this work, graphene interlayer-based epitaxy methods were employed to grow flexible inorganic GaN membranes with relatively inexpensive processes.

1.3 Inorganic flexible electronics fabrication

Flexible and stretchable optoelectronic devices are increasingly finding their purpose in modern devices. Thus, various fabrication strategies exist to meet this demand. One approach is to utilize intrinsically deformative organic materials, which are already employed in organic light-emitting diodes, organic photovoltaics, and organic thin-film transistors, among other devices [2, 28]. However, certain applications necessitate higher carrier mobilities and physical properties that do not degrade due to external environmental conditions. Consequently, inorganic optoelectronics emerges as a superior alternative [2].

Bulk structure growth methods cannot be directly applied to fabricate flexible inorganic electronics due to the significant mechanical mismatch between bulk inorganic semiconductors and flexible substrates. Bulk inorganic semiconductors are rigid and brittle. Fortunately, reducing thickness makes inorganic semiconductors flexible enough, as the critical bending radius is smaller for thin films than for bulk materials [3]. These thin layers can be transferred onto flexible substrates, creating flexible electronics. Flexibility can be further increased through wavy structure design, serpentine interconnection, or strain isolation. The thin inorganic film fabrication strategies involve epitaxial lift-off techniques using a chemically etched sacrificial layer, optically induced separation between the epilayer and substrate [4], brute-force mechanical spalling using a metal stressor layer, and 2D material-assisted layer transfer with a metal stressor [3]. This work focuses on the growth of thin films and the 2D material-assisted separation from the growth substrate.

1.3.1 Electrochemical exfoliation assisted by 2D materials

Assisted by 2D materials, layer transfer with a metal stressor stands out from other methods by offering superior efficiency in both time consumption and the smoothness of the transferred layer. In this technique, a stressor is deposited onto a weakly bonded epitaxial layer. The induced stress facilitates the peeling off the weakly bonded layer (see Figure 5).

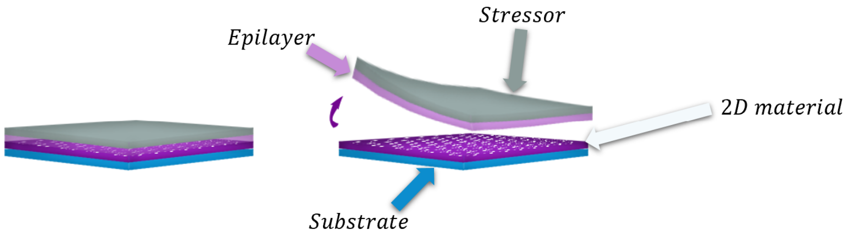

Figure 5: 2D material-assisted epitaxial layer exfoliation.

Compared with spalling from a bulk substrate with a metal stressor or laser-induced damage transfer, the exfoliated surfaces are smoother, and the substrate can be reused several times [3]. However, 2D material-assisted layer transfer has its drawbacks, such as the preparation of 2D materials, optimization of growth processes, and stressor deposition. Thus, it is important to optimize the growth process and deposit the stressor most efficiently. Electrochemical layer deposition is a perfect technique for stressor deposition as it is inexpensive, and the deposited layers can be characterized by modifiable strains based on selected electrolyte and electrochemical deposition parameters.

Principle of Electrodeposition

Electrodeposition technology, also known as electroplating, involves depositing a metallic coating onto a conductive substrate through the electrochemical reduction of metal ions from an electrolyte. In this process, the electrolyte is a conductive ionic liquid, where the metal species to be deposited are either dissolved in a suitable solvent or brought to a liquid state to form a molten salt.

Generally, the electroplating process consists of an electrolyte containing metal ions, the immersion of the sample to be coated (which acts as one of the electrodes), and a counter electrode usually made from the same metal as the coating to be deposited. If the counter electrode material matches the planned coating material, it assists in compensating ions involved in the electrolyte [29]. Both electrodes are connected to an external power supply to enable the current flow. The object to be coated is connected to the negative terminal of the power supply, while the counter electrode is connected to the positive terminal. In this setup, metal ions are reduced to metal atoms, eventually forming a deposit on the cathode surface.

A simplified electrolysis setup for nickel (Ni) coating is depicted in Figure 6.

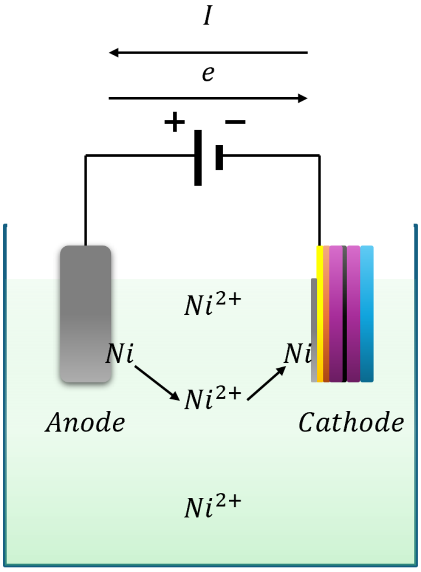

Figure 6: Simplified schematic of Ni electroplating on $Au/Ti/GaN/graphene/GaN/Al_2O_3$ sandwich type sample in an unspecified electrolyte.

The primary process occurring, regardless of the electrolyte type, can be explained through Faraday's laws of electrolysis. The equation represents the process reaction for metal formation [29]:

$$(M_xL_y)^z + nxe \rightarrow xM^0 + yL, \tag{1}$$

where M represents a metal ion, L denotes a molecule, ion, or radical, e stands for elementary charge, n is the net number of electrons transferred per deposited metal atom, and z indicates the electric charge of the electroactive species in electron units. M and L together form complexes that participate in charge transfer. Equation 1 can be understood as the transfer of a charge of ne needed to deposit one metal atom. The formation of one mole of the desired metal requires $N_A ne = nF$ coulombs of electricity, where N_A is Avogadro's number and $F = N_A e$ is Faraday's constant.

Consequently, the mass (m) of deposited metal can be evaluated using Faraday's law [29]:

$$m = \frac{QA}{nF} \tag{2}$$

In equation 2, Q represents the net charge passed through the circuit, and A is the atomic weight of the metal. The equation plays a crucial role in determining the amount of deposited material. However, in practical scenarios, it's more common to calculate the thickness of electroplated metal (h) over time (t) rather than its mass. This can be accomplished by considering that $h = m/Sd$ and $Q = It$, where S represents the surface area, d is the density, and I stands for the current. Thus, by rearranging equation 2, we derive:

$$h = \frac{(I/S)At}{dnF} \tag{3}$$

This equation is frequently used for the initial estimation of electroplated metal thickness. However, the actual thickness may vary due to the imperfect efficiency of the electrodeposition process.

Selection of electrolyte

The properties of the deposited metal coating largely depend on the chosen electrolyte and various conditions, including current density, temperature, deposition time, the distance between electrodes, and their shapes. In this study, the objective of the metal coating was to exfoliate weakly bonded material on graphene. To ensure successful liftoff of materials grown via 2D interlayer, depositing metal layers with internal residual stress is crucial. Ni is commonly employed for this purpose. Ni can exhibit varying residual stress levels depending on the electrolyte type and electroplating conditions.

Electroplating with Watts nickel solution is commonly employed to produce strained nickel deposits. Previous research has shown that such a solution without additives can exhibit tensile stress in the order of 10^2 MPa [30]. Moreover, the stress levels can be further adjusted with additives. Hence, for our study, we chose to employ this electrolyte for electroplating since similar stress values were reported by Hoe-Min Kwak et al. in GaN exfoliation using the Ni stressor [23].

During electroplating, minor stress adjustments can be achieved by fine-tuning parameters such as thickness, electrode spacing, pH, and current density [30, 31]. For more significant adjustments, organic additives like saccharin ($C_7H_5NO_3S$) can be introduced [32–34]. The electrolyte used in our study was a Watts type similar to that utilized by Nakamura et al. for continuous layer plating [33].

The chosen electrolyte, in addition to deionized water, consists of several compounds, each serving a specific role [30]:

- **Nickel Sulfate Hexahydrate** ($NiSO_4 \cdot 6H_2O$): This compound serves as the primary source of nickel ions (Ni^{2+}). When dissolved in water, $NiSO_4 \cdot 6H_2O$ dissociates into nickel and sulfate ions.

- **Nickel Chloride Hexahydrate** ($NiCl_2 \cdot 6H_2O$): This compound acts as a secondary source of nickel ions in the electrolyte solution. Additionally, it enhances solution conductivity, thereby reducing voltage requirements. It also plays a crucial role in improving the dissolution of nickel anodes.

- **Boric acid** (H_3BO_3): Boric acid acts as a buffer to maintain the pH of the electrolyte solution within the desired range. Since the cathode efficiency is less than 100%, pH fluctuations may occur due to the discharge of hydrogen ions to liberate hydrogen gas. Boric acid helps limit these fluctuations, simplifying pH control.

- **Saccharin** ($C_7H_5NO_3S$): Saccharin serves as a brightening agent and an additional stress controller. A small concentration of saccharin (approximately 0.0 to 0.3 g/l) reduces tensile stress by facilitating co-deposition in grain boundaries of sulfur and nitrogen from saccharin molecules. Additionally, saccharin can alter the surface morphology, hardness, cathodic current efficiency, and cathodic polarization behaviors of the plating solution [32, 33].

- **Propargyl alcohol** (C_3H_4O): Propargyl alcohol acts as a wetting agent and an additional suppressor of hydrogen evolution during the plating process. It promotes uniform deposition of nickel on complex or irregularly shaped substrates while mitigating the formation of hydrogen gas bubbles [33].

During electrochemical deposition using the Watts solution, stress (σ) can originate from several factors: 1) lattice mismatch at the interface between the coating and substrate, 2) differences in the coefficient of thermal expansion, and 3) residual or intrinsic stress resulting from specific plating conditions and bath composition [35].

In lift-off experiments, the functionality of the stressor is attributed to residual stress. Generally, the mechanisms underlying residual stress differ for each metal deposit, but some main tendencies can be observed.

At the beginning of electrochemical deposition (around 2 seconds into the process [31]), compressive stress arises during the island growth stage due to surface capillary forces acting on isolated island clusters. After a few seconds (approximately 10 seconds into deposition [31]), the nature of stress shifts to tensile stress. This type of stress emerges as the cluster size increases, causing them to collide with each other and undergo coalescence. In the final stage, when the film is relatively flat, the stress typically stabilizes at a constant value.

For successful thin film exfoliation, the generation of residual tensile stress is necessary. The mechanism for generating tensile stress was initially proposed by R.W. Hoffman [36] and further elaborated by E. Chason [37]. These models attribute the accumulation of stress to the decrease in surface energy as non-connecting individual island clusters merge into a continuous layer with grain boundaries. Figure 7 presents a simplified depiction of this process.

In Figure 7, separate islands are depicted as cuboids with lateral dimensions L, a height h, and a spacing between islands equal to d. As the islands grow, the spacing between them is reduced, and

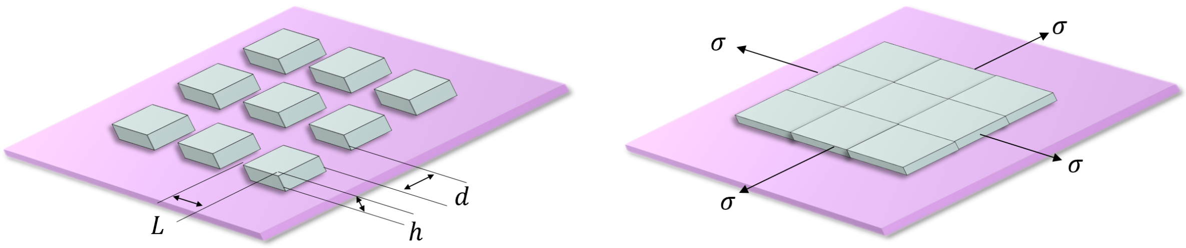

Figure 7: A simplified scheme of biaxial stress generation. Only individual island clusters are visible in the left image, experiencing strain from surface capillary forces. On the right side, these individual clusters merge into a continuous layer with grain boundaries interspersed among them. Predicting stress becomes more complex as grain boundaries exhibit various shapes. Illustration adapted from literature [37]

eventually, they connect, forming a continuous layer with grain boundaries, as shown in Figure 7(b). In a simplified scenario, such connections induce a uniform biaxial strain in the island of d/L. Since the strain is equal in both in-plane directions, this process increases the strain energy $\left(U = \frac{V\sigma^2}{2E}\right)$ in the island by [37]:

$$\Delta E_{strain} = hL^2 \frac{\sigma^2}{(\frac{E}{1-\nu})}, \tag{4}$$

where E - Young's modulus and ν is Poisson's ratio. Conversion of the free surface at the edge of the island into a grain boundary correspondingly decreases the island's energy by [37]:

$$\Delta E_{interface} = -4Lh\Delta\gamma \tag{5}$$

where $\Delta\gamma$ represents the difference between γ_s, the interfacial energy of the free surface, and $\frac{1}{2}\gamma_{gb}$, the energy of the grain boundary. Given that the condition $|\Delta E_{interface}| > |\Delta E_{strain}|$ must be satisfied for grain boundary formation, a critical value for tensile stress can be predicted as:

$$\Delta\sigma_{crit} = -2\left(\frac{E}{1-\nu}\right)^{\frac{1}{2}}\left(\frac{\Delta\gamma}{L}\right)^{\frac{1}{2}} \tag{6}$$

The equation 6 suggests that layers with smaller grains will experience higher tensile stress, as indicated by the inverse relationship with $L^{-\frac{1}{2}}$ value. The size of the islands or crystallites (L) can be estimated from the full width at half maximum (FWHM) intensities of X-ray diffraction (XRD) peaks using the Scherrer equation, which is commonly employed for calculating crystallite size [38]:

$$L = \frac{K\lambda}{\beta\cos\theta}, \tag{7}$$

where λ is the X-ray wavelength, β is FWHM of the diffraction peak from small crystallite in radians and K is a constant related to crystallite shape, normally taken as 0.9.

This model can be explained simply by considering atoms at the edges of layer terraces. During the layer formation stage, when two adjacent grains come close to each other, they tend to bond even if this bond introduces stress (shortened or prolonged bond length compared to an unstressed state). This bonding occurs if the energy gained from the bond outweighs the strain energy induced in the layer.

On the other hand, compressive stress typically arises from a boundary insertion mechanism. This stress is generated by the diffusion of atoms into the grain boundary during growth. The driving force behind this compressive stress lies in the non-equilibrium conditions present on the surface during deposition, which cause an increase in the chemical potential of adatoms relative to equilibrium conditions [37].

1.4 Material characterization methods

For successful functional device fabrication, it is essential to examine fabricated structures at every step of the manufacturing process. In this work, scanning electron microscopy (SEM), Raman spectroscopy, XRD measurements, and simple inspection using an optical microscope were employed to obtain knowledge about materials and processes during GaN membrane fabrication.

1.4.1 Scanning electron microscopy

The SEM has an identical primary function as the optical light microscope - to enlarge small features or objects that are hardly seen by the naked eye. However, the SEM offers much greater resolving power than an optical microscope. A higher resolving power comes from accelerated electrons exhibiting wave-like properties, with their effective wavelength being much shorter than that of visible light. Thus, the Abbe limit - the minimum distance between two points that can be resolved is also smaller. The wavelength of electrons in an SEM is typically on the order of a few picometers and the minimal revolved feature dimensions vary around 1 nm [39].

The SEM instrument and its operation can be divided into several components: an electron gun, electromagnetic lenses, scan coils, the specimen chamber with various detectors, and computer/electronic controls. An electron gun generates a beam of electrons, which is further accelerated by applied voltage. Electromagnetic lenses focus the beam into a probe of a small diameter. Subsequently, scan coils move the probe across the sample's surface in a column-raster pattern. The incident electrons can penetrate a few microns into the surface of a bulk sample depending on an applied voltage. Upon the interaction between the electron beam and the sample atom, a variety of consequential events occur, such as the generation of Auger electrons, secondary electrons, electron backscattering, as well as the emission of characteristic X-rays, Bremsstrahlung X-rays, and fluorescence [39]. The detection of these signals is important for material characterization with SEM. Figure 8 depicts secondary electron and characteristic X-ray generation.

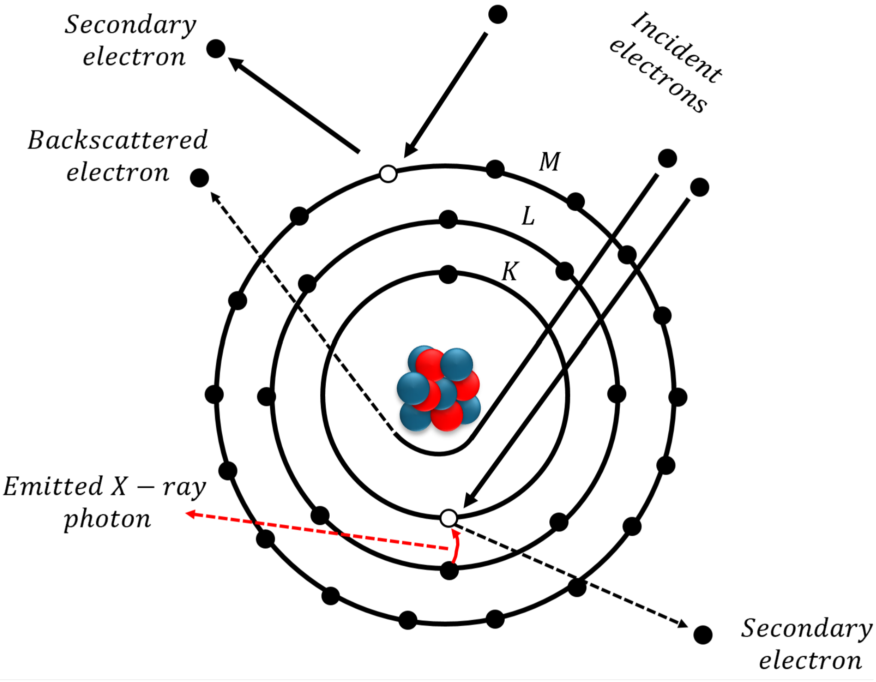

Figure 8: Representation of the interaction between an electron beam and the K orbital electron. One possibility is that the incident electron can be elastically scattered. Another possibility is that the electron can be knocked out and ejected from the atom, thus creating a vacancy. The created vacancy in the K shell can be filled by an electron from a higher energy shell (for example, the L shell). This filling process is accompanied by the release of an X-ray photon. Transitions from other shells to fill the vacancy are also possible.

Detected secondary electrons are used for imaging topographic contrast, while backscattered electrons can provide additional information about compositional contrast because the electron yield is related to the atomic number. Energy dispersive X-ray spectrometry (EDS) offers information about the sample's chemical composition through the emitted characteristic X-rays.

Therefore, SEM is a popular tool that provides information about the surface or near-surface structure and its composition. In this work, *Apollo CamScan 300* SEM was used to characterize the samples.

1.4.2 Raman spectroscopy

Raman spectroscopy is a vibrational spectroscopy technique based on molecules' inelastic scattering of light. When a molecule interacts with incident light, it becomes excited, which distorts the molecule's electron cloud. The distorted cloud may either return to its original ground state or a higher/lower vibrational state. The first scenario is known as elastic scattering or Rayleigh scattering, while the second is called the inelastic scattering of radiation, also known as Raman scattering. Figure 9 illustrates the differences between Rayleigh and Raman scattering.

During Raman spectroscopy experiments, the Stokes and anti-Stokes lines are measured. Each material has a unique characteristic spectrum corresponding to transitions between vibrational states. These spectra provide information about material composition, strain, defects, and, in some

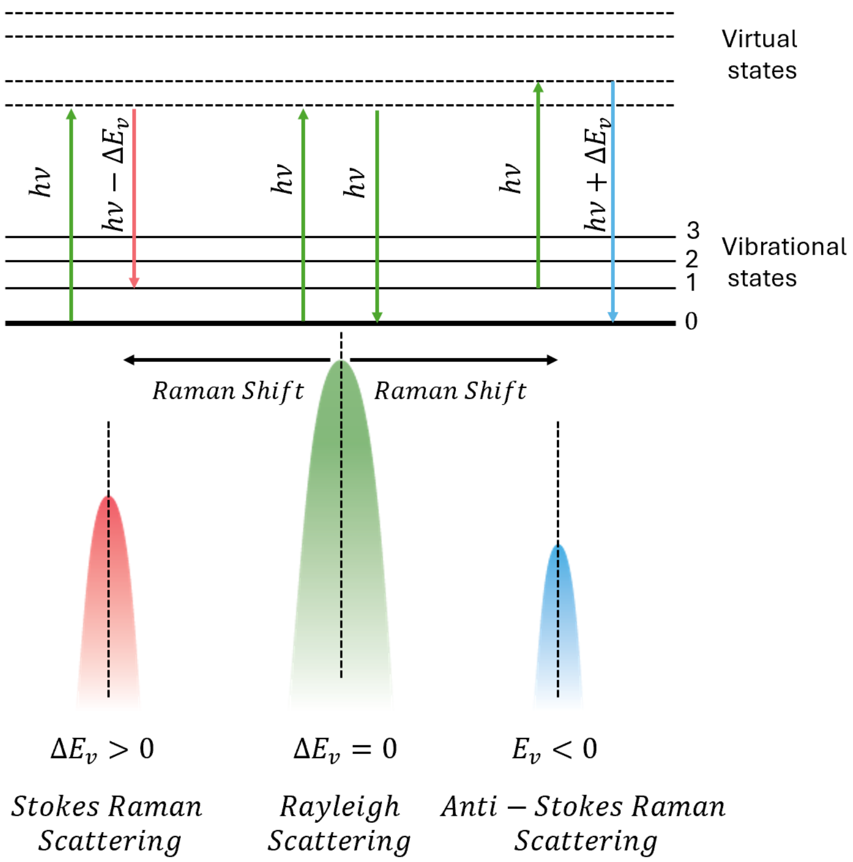

Figure 9: Schematic presentation of the quantum description of the Rayleigh, Stokes, and anti-Stokes scattering in terms of energy and intensity difference. Illustration adapted from literature [40].

cases, even the number of atomic layers. In this work, the latter is most important.

A brief overview of the theory behind the Raman effect can be expressed from classical physics and quantum mechanics viewpoint.

In the classical physics-based model, a molecule with a polarizability tensor $\overleftrightarrow{\alpha}$ is considered. When such a molecule is placed in a static electric field $\vec{E}$, it gets polarized and an electric dipole moment is induced:

$$\vec{\mu} = \overleftrightarrow{\alpha}\, \vec{E} \tag{8}$$

Now consider a sample which is subjected to a beam of monochromatic radiation of frequency ν. The electric field experienced by the molecules oscillates with the same frequency:

$$\vec{E}(t) = \vec{E}_0 \sin(2\pi\nu t) \tag{9}$$

If the molecule is undergoing an internal vibration with a frequency ν_i, the polarizability can be described by the following expression:

$$\overleftrightarrow{\alpha} = \overleftrightarrow{\alpha}_0 + \overleftrightarrow{\alpha}_1 \sin(2\pi\nu_i t) \tag{10}$$

Hence, the induced dipole moment is given by:

$$\begin{aligned}\vec{\mu} &= (\overset{\leftrightarrow}{\alpha}_0 + \overset{\leftrightarrow}{\alpha}_1 \sin(2\pi\nu_i t))\vec{E}_0 \sin(2\pi\nu t) \\ &= \overset{\leftrightarrow}{\alpha}_0 \vec{E}_0 \sin(2\pi\nu t) + \frac{1}{2} \overset{\leftrightarrow}{\alpha}_1 \vec{E}_0 [\cos(2\pi(\nu + \nu_i)t) - \cos(2\pi(\nu - \nu_i)t)]\end{aligned} \tag{11}$$

Thus, along with the elastic component with frequency ν, the scattered radiation will contain inelastic components with frequency $\nu \pm \nu_i$.

For the quantum mechanical treatment of the problem, consider a molecule that absorbs a laser photon with energy $h\nu$. This absorption excites the molecule to a virtual electronic energy level; the photon's re-emission leads to scattering. The final state of the molecule has the same electronic energy as the initial state, but the vibrational energy E_ν might be changed. There are three possible cases:

- **Rayleigh scattering**: the total energy of the molecule remains the same ($\Delta E_\nu = 0$) and the frequencies of the incident and emitted photons are equal ($\nu = \nu'$).
- **Stokes Raman scattering**: vibrational energy of the molecule becomes higher after scattering ($\Delta E_\nu > 0$).
- **Anti-Stokes Raman scattering**: vibrational energy of the molecule becomes lower after scattering($\Delta E_\nu < 0$).

Graphene and graphene-like materials have well-defined characteristic Raman spectra. The dominant features in such spectra are the so-called G band appearing at 1582 cm^{-1} and the 2D band at about 2700 cm^{-1} [41]. In the case of a disordered/defective sample, two new modes appear. Disorder-induced D-band, at about half of the frequency of the 2D and D' disorder-induced feature, appears at $\sim cm^{-1}$. Usually D' feature overlaps with the G band.

The intensity ratio between 2D and G bands as the shape of the 2D band can be used for the evaluation of several atomic graphene layers approximately up to 7 [42]. As the layer number increases, the Raman spectrum starts to resemble bulk graphite. Furthermore, a double-resonance model can be used to determine the number and position of the elemental peaks within the 2D band that are related to the number of atomic planes from the experimentally measured sample. The shape sensitivity is used to evaluate a number of graphene atomic layers. The change in the intensity ratio between 2D and G bands with the increasing number of layers was determined empirically and is used as an additional verification of the number of layers. Usually, this ratio is 2 for monolayer graphene, however, it can vary based on the experimental procedure [24].

A confocal Raman microscope working with a 532 nm laser was used in the work.

1.4.3 X-ray diffraction

To produce high-quality devices from epitaxial thin films, their quality must be evaluated. The crystal quality can be understood as the deviation from perfect crystal structure due to appearing stresses and defects within the layer. In the presence of crystallographic defects, macrostrains form in the crystals leading to local changes of d-spacing between crystallographic planes or planes that are locally rotated (bent). Furthermore, epitaxial thin films have a relationship with a substrate. In heteroepitaxy, bonding between an epilayer and a substrate induces additional stresses. Various changes in crystal lattice, d-spacing, plane orientation, and even an approximation of layer thickness can be measured by XRD. Deviation from perfect crystal structure leads to broadening the diffraction peaks [43].

X-ray diffraction can be understood by interpreting Bragg's law in real space. In this model, X-rays are scattered from neighboring planes with spacing d. The constructive interference will appear when the path difference between scattered rays is equal to the integer number of wavelength $n\lambda$. In this case, the intensity of diffracted light will be at its maximum. This condition is described by Bragg's Law and holds true for incident and diffracted light beams with equal angles relative to the planes:

$$n\lambda = 2d\sin\theta, \tag{12}$$

where θ is the angle between the plane and x-ray radiation. This type of scattering is called Bragg reflection since the angle of incidence is equal to the angle between planes and the diffracted beam (see Figure 10). Furthermore, the order parameter n is considered to be 1 because the higher-order diffractions are equivalent to the first-order diffraction but from planes with integer spacing (d/2, d/4, d/6...). Thus, the order parameter is accounted for in the spacing, and Bragg's law expression for crystallography is often expressed as:

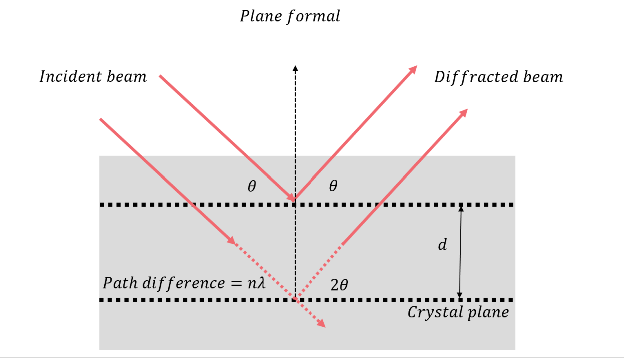

Figure 10: Real space illustration of Bragg's law. Illustration adapted from literature [43].

$$\lambda = 2d\sin\theta. \tag{13}$$

The experimental measurements often are interpreted using the reciprocal space model of Bragg's law. In this model, beams are represented by the wave vectors: incident beam $|\vec{K}_1| = 1/\lambda$ and detected beam $|\vec{K}_2| = 1/\lambda$. The difference of these vectors defines the scattering vector $|\vec{Q}| = |\vec{K}_2 - \vec{K}_1|$. As the angle between $|\vec{K}_1|$ and $|\vec{K}_2|$ is 2θ, thus, the scattering vector $|\vec{Q}| = 2\sin\theta|\vec{K}_1|$. This is a fundamental experimental condition, where Bragg reflection from reciprocal planes can only occur when the scattering vector Q is equal to reciprocal lattice vector $\vec{d}^* \rightarrow |\vec{Q}| = 1/\mathrm{d} = |\vec{d}^*|$.

The classical X-ray measurement scheme is rather primitive, consisting of several key elements: sample illumination by X-rays, diffraction by the mounted sample, and collection of diffracted beams by a detector. While it may sound straightforward in principle, precise control of the mounted sample and goniometer mechanisms allows for the application of various measurement methods.

$2\theta/\omega$ scan is one of the most popular XRD measurement methods. During the $2\theta/\omega$ scan only the length of the scattering vector changes but not its direction. The scan is done by selecting $\delta 2\theta$ step value twice as large as the step of change in the incident beam angle, $\delta 2\theta = 2\delta\omega$ (Figure 11). The described measurements are used to determine the crystal planes that are perpendicular to the scattering vector. During the measurement, the Bragg diffraction 2θ angles are measured, from which the interplanar distances d of the material can be estimated.

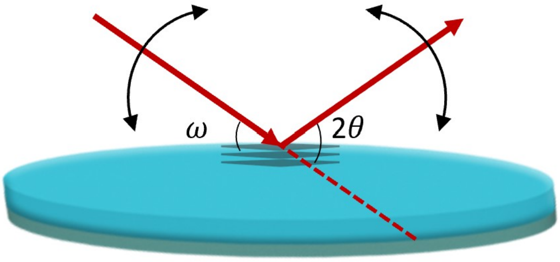

Figure 11: Illustration of $2\theta/\omega$ scan principle.

The other two popular XRD measurement methods are called rocking curve and ϕ scans. The rocking curve measurement or ω scan is performed by rocking the sample while the detector is fixed at a specific 2θ angle. From the rocking curve diffractogram, the preferred crystal plane orientation in the sample can be analyzed. Recorded XRD intensity is used to check the FWHM intensity of the peak which gives insight into preferred orientation distortion. During ϕ scans, the incidents ω and diffraction angles θ are fixed, and only a sample is rotated around an azimuth called the ϕ axis. The angle ϕ usually varies from 0 to 360 deg. By collecting X-ray diffraction data at different ϕ angles, we can evaluate the parallelism of the selected planes and determine the orientation of the crystal lattice. These methods are used to obtain diffraction patterns from depths up to several microns. To avoid the signal from the substrate and enhance the signal from the thin film itself, a 2θ scan with a fixed grazing angle of incidence can be conducted.

XRD can also be utilized for residual stress measurement in both monocrystalline and polycrystalline materials. In monocrystalline materials, the stress in one direction can be easily evaluated through $2\theta/\omega$ scans by determining the change in interplanar distance from the measured Bragg's angle. Subsequently, strain and stress in other directions can be evaluated by incorporating Poisson's ratio ($-\nu\epsilon_z = \epsilon_y = \epsilon_x$). For polycrystalline materials, a $2\theta/\psi$ scan is typically employed. In this method, multiple $2\theta/\omega$ scans are performed at different ψ, where ψ defines the inclination of plane in respect to the surface.

In an unstrained polycrystalline material, the spacing between lattice planes remains independent of the tilt/rotation of the planes and can be measured using Bragg's law 13. If the specimen is stressed due to elastic deformation, the interplanar spacing will depend on the crystallite orientation. In cases of stretching, the interplanar distance will increase for planes perpendicular to the direction of tension and decrease for parallel ones (see Figure 12).

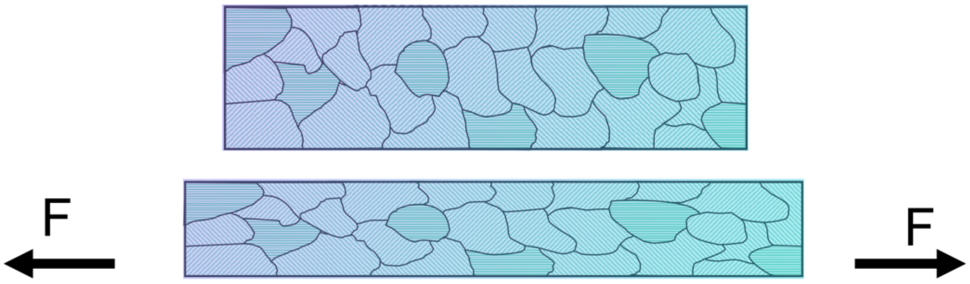

Figure 12: The top polycrystalline layer is not affected by applied force, the bottom layer is affected by external tension.

The interplanar distance can be easily estimated by measuring the Bragg angle. Varying the inclination of the specimen and measuring this angle determines the strain [44]. The scheme of such a measurement is shown in Figure 13.

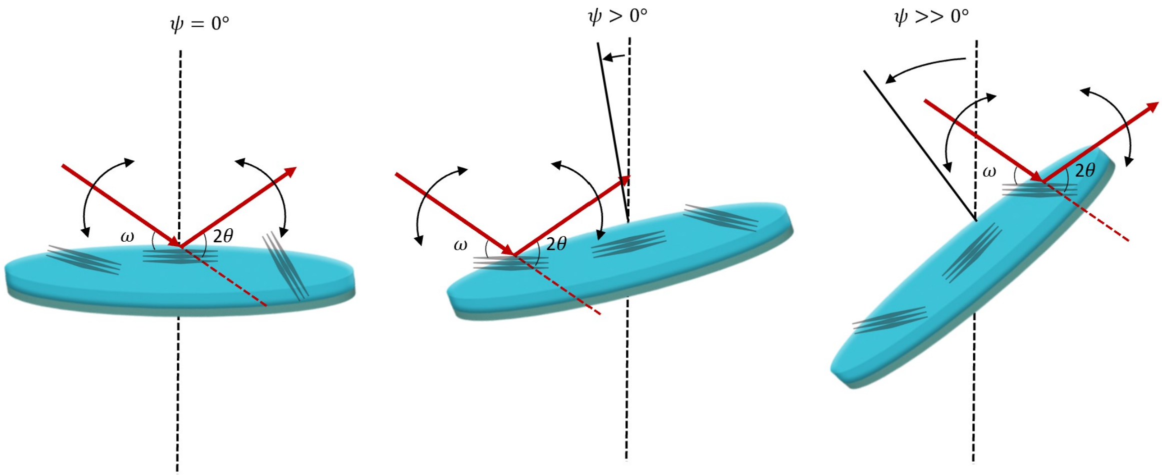

Figure 13: The principle of $2\theta/\psi$ residual stress measurement involves performing $2\theta/\omega$ scanning for crystallites with planes whose scattering vector matches normal to the plane surface. Subsequently, the sample is tilted, and new reflections are recorded for the same planes but in tilted crystallites. The interplanar distance of planes depends on the sample tilt, as different stress components come into play.

As mentioned previously, diffraction peak results from x-ray scattering by periodic lattice. The same peak from a specific plane group will shift due to a change in the lattice spacing. Thus, by measuring the change in diffraction peak position, the change in interplanar distance d can be used to calculate the degree of strain within a crystalline material [44]:

$$\epsilon = \frac{d_n - d_0}{d_0}. \tag{14}$$

In equation 14, d_0 is crystal lattice spacing without stress and d_n is crystal lattice spacing including stress.

Including expression 14 into Hook's law, the amount of stress σ can be determined from the strain values [44, 45]:

$$\left(\frac{d_\psi - d_0}{d_0}\right) = \frac{1+\nu}{E}\sigma \sin^2 \psi, \tag{15}$$

where d_ψ is the lattice spacing at each ψ angle. The common method for stress determination requires a plot of the different d_ψ against $\sin^2 \psi$, where the slope value indicates stress [44, 45].

In this work, residual stress measurements using XRD measurements were performed using a *Rigaku SmartLab* diffractometer.

2 Experimental methods

To fulfill the goal of this work, the experimental methods and results are discussed based on the tasks created and the following workflow, which includes the template for 2D material-assisted epitaxy preparation, graphene transfer, GaN growth on graphene, stressor deposition on arbitrary substrates, and membrane exfoliation. The workflow is depicted in Figure 14 for clarity.

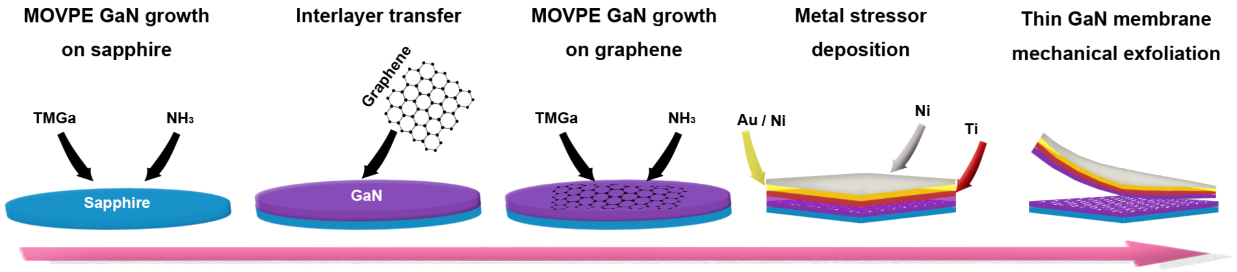

Figure 14: Key steps applied for GaN membrane exfoliation. A brief process description is provided above the images.

Preparation of templates for 2D material-assisted epitaxy

A templates must be prepared for further 2D material-assisted epitaxy experiments. In this study, we selected one of the most economically efficient solutions: a GaN/sapphire substrate for 2D material-assisted epitaxy of GaN. Our group had already mastered the preparation of such substrates, as detailed by *K. Badokas* [15]. Consequently, in the MOVPE reactor, only the initial 2-inch (5.08 cm) c-plane Al_2O_3 substrate needed to be introduced, and the operator simply ran a pre-existing, functional program with specific growth parameters.

The key aspects outlined in the code included growth temperature, pressure regulation, control of precursor and dilution line flows, and timing management. The initial GaN on Al_2O_3 growth process involved annealing in a H_2 atmosphere at 1080°C for 300 seconds. This step ensured the removal of most contaminants from the sapphire surface and the partial elimination of oxygen to facilitate nitride layer formation. Following a multi-step recipe, the GaN film was subsequently grown. This process began with low-temperature nucleation, followed by GaN film growth at an elevated temperature in the range of $1090 - 1120$°C. The growth was facilitated with an NH_3 flow rate of 1.1×10^{-1} mol/min and TMGa of 1.6×10^{-4} mol/min at 150 mbar.

After growth, GaN quality was evaluated by XRD.

Graphene transfer

Graphene transfer on GaN/Al_2O_3 substrates was a crucial step in the 2D material-assisted GaN lift-off procedure. Graphene was transferred using two methods, as illustrated in Figures 15 and 16.

The first transfer method utilized in this study is known as the wet transfer method. The steps involved in this transfer method are illustrated in Figure 15.

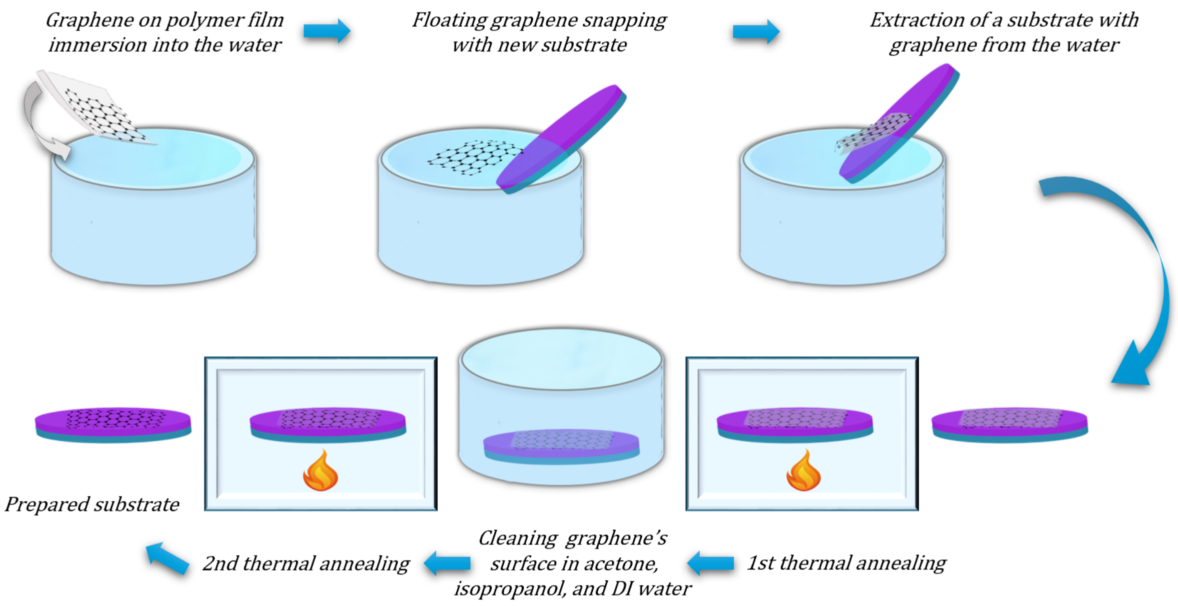

Figure 15: The illustration depicts the steps involved in transferring graphene from a holder substrate using water.

The depicted procedure began by immersing a support film containing a sacrificial layer/graphene sample from *Graphenea* manufacturer into DI water at 45 °C. When the film was submerged in water, the sacrificial layer/graphene separated from the polymer film and floated on the water surface due to graphene's hydrophobic properties. Next, the GaN/sapphire substrate was introduced into the DI water, and the floating sacrificial layer/graphene was snatched. After capturing the graphene, the substrate was removed and allowed to dry at room temperature. To eliminate any remaining water and ensure better adhesion of the graphene to the substrate, rapid thermal annealing was conducted for 30 minutes at 150°C in an N_2 atmosphere, followed by vacuum exposure for 22 hours.

Following annealing, the sacrificial layer was cleaned in acetone and isopropanol for 30 minutes each, and then the sample was rinsed in DI water. Lastly, a second thermal annealing step at 300°C in vacuum was performed for 6 hours to completely remove any remaining sacrificial PMMA residues. After this process, the substrate was prepared for 2D material-assisted epitaxy.

The alternative method, termed "transfer with a laminator," follows the steps outlined in Figure 16. This approach is suitable for large-area transfers, which is advantageous for covering entire growth substrates. Additionally, the transfer process is less expensive compared to the wet method.

The depicted procedure began with copper foils containing CVD-grown graphene undergoing overnight oxidation in deionized (DI) water. Soaking in DI water oxidatively decoupled the graphene from the catalyst surface. The graphene on copper foil was obtained from the manufacturer, *Grolltex*. Subsequently, the soaked foil was dried in a room temperature environment and laminated at 112°C, with a speed of 16 cm/min, using a commercial *Sky 335R6* hot-roll laminator onto commercially available polyvinyl alcohol (PVA) sheets pre-cleaned with isopropanol. These PVA sheets came with supporting paper that was removed prior to the cleaning process.

After lamination, the PVA film with graphene and copper foil was baked on a hot plate at 112°C for 1 minute to enhance graphene adhesion to the PVA. Subsequently, mechanical delamination of

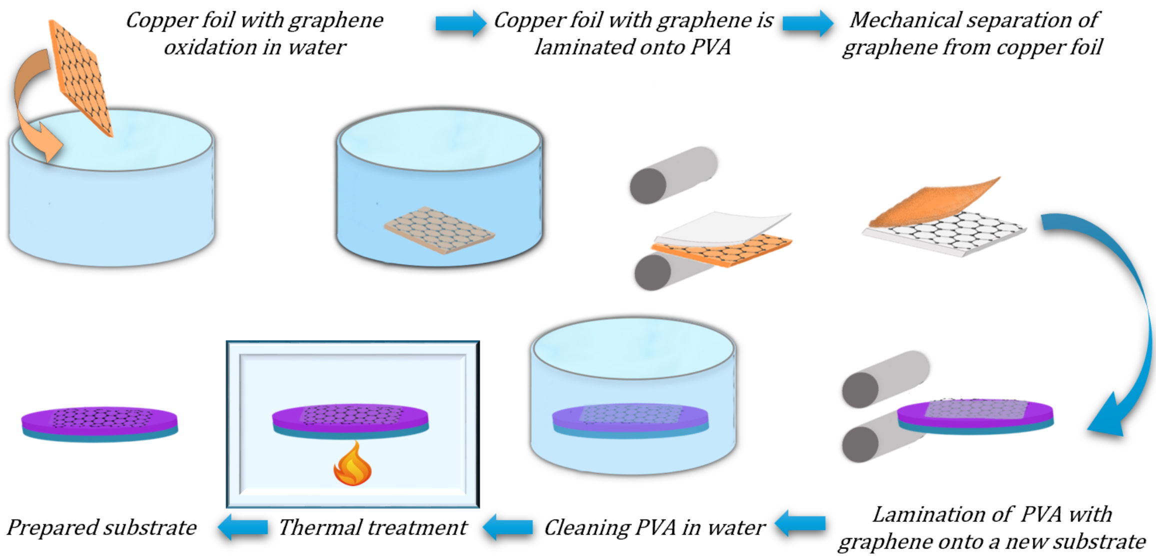

Figure 16: Illustration depicts the steps involved in transferring graphene using a laminator.

the copper foil from the PVA was performed, leaving the graphene on the PVA. Following this step, the graphene was available on a flexible polymer substrate and was ready to be transported onto an arbitrary substrate.

Transfer was achieved by laminating the PVA/graphene film onto a GaN/sapphire substrate under the same lamination conditions and baking it on a hot plate. Lastly, the support paper was peeled off, leaving only the PVA with graphene on the substrate. The next step involved the removal of the PVA, which was accomplished using DI water and thermal annealing.

The quality of transferred graphene was examined using Raman spectroscopy, scanning electron microscopy (SEM), and optical microscopy.

GaN growth on graphene using MOPVE

The second GaN epilayer growth with MOPVE was conducted either on graphene or its flakes deposited on GaN/Al_2O_3. GaN growth on graphene, transferred using wet and laminator methods, was performed in several ways, including low-temperature GaN (LT-GaN) and high-temperature GaN (HT-GaN). Initially, the focus was on growing LT-GaN to gain hands-on experience with 2D-material-assisted epitaxy. Maintaining lower growth temperature is crucial for preserving graphene, as higher temperatures can lead to its deterioration or even elimination [46]. In the latter case, the epitaxy of the 2D material vanishes, and conventional epitaxy dominates.

The primary growth parameters for LT-GaN growth include a nucleation and layer formation temperature of 700°C, which is reached over 450 s. The growth process occurs over 30 minutes in an atmosphere of N_2, with an NH_3 flow rate of 8.0×10^{-2} mol/min and TMGa of 3.0×10^{-5} mol/min, under a pressure of 600 mbar. The choice of an N_2 atmosphere was intentional, as it is less aggressive (lower etching rate) compared to H_2 and better preserves the quality of graphene [46,47]. In one of the initial LT-GaN growth experiments on graphene flakes transferred using laminators, pre-treatment involved a 150 s TMGa flow at 8.0×10^{-2} mol/min before GaN growth. This pre-treatment aims to provide extra protection to graphene and reduce substrate deterioration that could potentially damage the graphene layer [48]. Growth characteristics are illustrated in the Results section (Figure 36).

Afterward, the LT-GaN growth was carried out on a wet-transferred graphene layer without TMGa pre-flow. The growth characteristics of this layer are presented in Figure 28.

In addition to the later growth, a high-temperature growth regime was added to the next sample (Figure 34). In this case, after the LT-GaN growth described above on wet-transferred graphene, a follow-up by 10-minute HT-GaN growth was conducted in a H_2 atmosphere at 1080°C. The growth process was facilitated with an NH_3 flow rate of 1.1×10^{-1} mol/min and TMGa of 1.6×10^{-04} mol/min at 150 mbar.

Several growths of HT-GaN were conducted subsequently with varying TMGa pre-flow times. HT-GaN growth started with low-temperature growth as described above, but with a shorter growth time (300 s) to form the initial GaN islands. This was followed by a temperature increase to 1120°C over 600 s. Afterward, during the first 2700 s at 150 mbar pressure, islands recrystallized and merged into continuous layers, followed by the growth of additional layers at 1120°C.

The corresponding grown materials were utilized for further exfoliation experiments.

Stressor deposition

To facilitate the exfoliation of GaN layers, a Ni stressor was electroplated. Before the electroplating process, copper test samples and two sets of samples, similar to those intended for exfoliation, were prepared with different preconditioning methods. The first set of samples contained 50 nm of Ti and 50 nm of Ni on top of GaN, while the second set had 50 nm of Ti and 50 nm of Au on top. These layers served as an adhesive/ohmic layer and a seed layer, respectively. Although the Ni option was more economical, it could oxidize and reduce the adhesion of the electroplated layer. Therefore, the Au alternative was also selected. These layers were deposited using electron-beam evaporation.

Subsequently, these samples were connected as the cathode in a self-made electroplating jig, and the electrical connection between the samples and the jig was verified using a multimeter. The distance between electrodes was 7 cm. The electroplating solution used was Watts, and its composition is described in more detail in Section 1.3.1. The temperature of the solution was maintained in the range of 40-55°C and its pH varied around 4. The electroplating current density was controlled by manually adjusting the power supply voltage. Current density, deposition time, and saccharine concentration in the electroplating solution were varied in order to deposit Ni layers with optimal residual stress.

After deposition, the coating surface was examined with SEM and a profilometer. The residual stress of Ni was also evaluated using XRD.

3 Results and discussion

Results are discussed following the same workflow steps depicted in Figure 14 - starting with the template for 2D material-assisted epitaxy preparation and finishing with the analysis of exfoliated membranes.

3.1 Templates for 2D material-assisted epitaxy preparation

Firstly, in order to enter the remote homoepitaxy regime or pinhole-based epitaxy, or at least the lateral overgrowth regime, where the growth of the epilayer on the 2D material is influenced by the substrate beneath the graphene (2D material), a high-quality substrate was prepared. The growth procedure for such substrates was previously documented and presented by *K. Badokas* [15]. To ensure that the quality remained consistent, the newly prepared substrates for the following experiments were studied employing XRD. Rocking curve measurements were conducted for the GaN (0002) reflection and are presented in Figure 17.

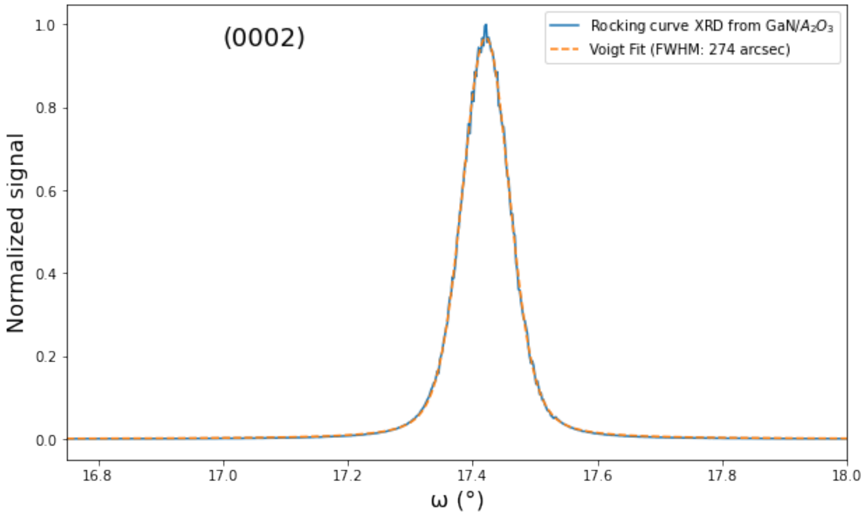

Figure 17: XRD ω scan of GaN on an Al_2O_3 substrate serving as a reference for subsequent epitaxy experiments.

The FWHM value was computed by applying Voigt fit to the measured rocking curve data. The calculated FWHM value was under 300 arcsec, indicating that the substrates exhibited usual crystalline quality [15,49] for GaN grown on sapphire and can be further used in exfoliation experiments.

3.2 Graphene transfer

To enable the 2D material-assisted epitaxy regime, graphene was transferred onto GaN/Al_2O_3 substrates. Graphene was transported using two strategies described in Section 2. Let's first review the results of wetly transferred graphene. The transferred graphene surface and the boundary area without graphene were examined with SEM (see Figure 18 (a) and (b)).

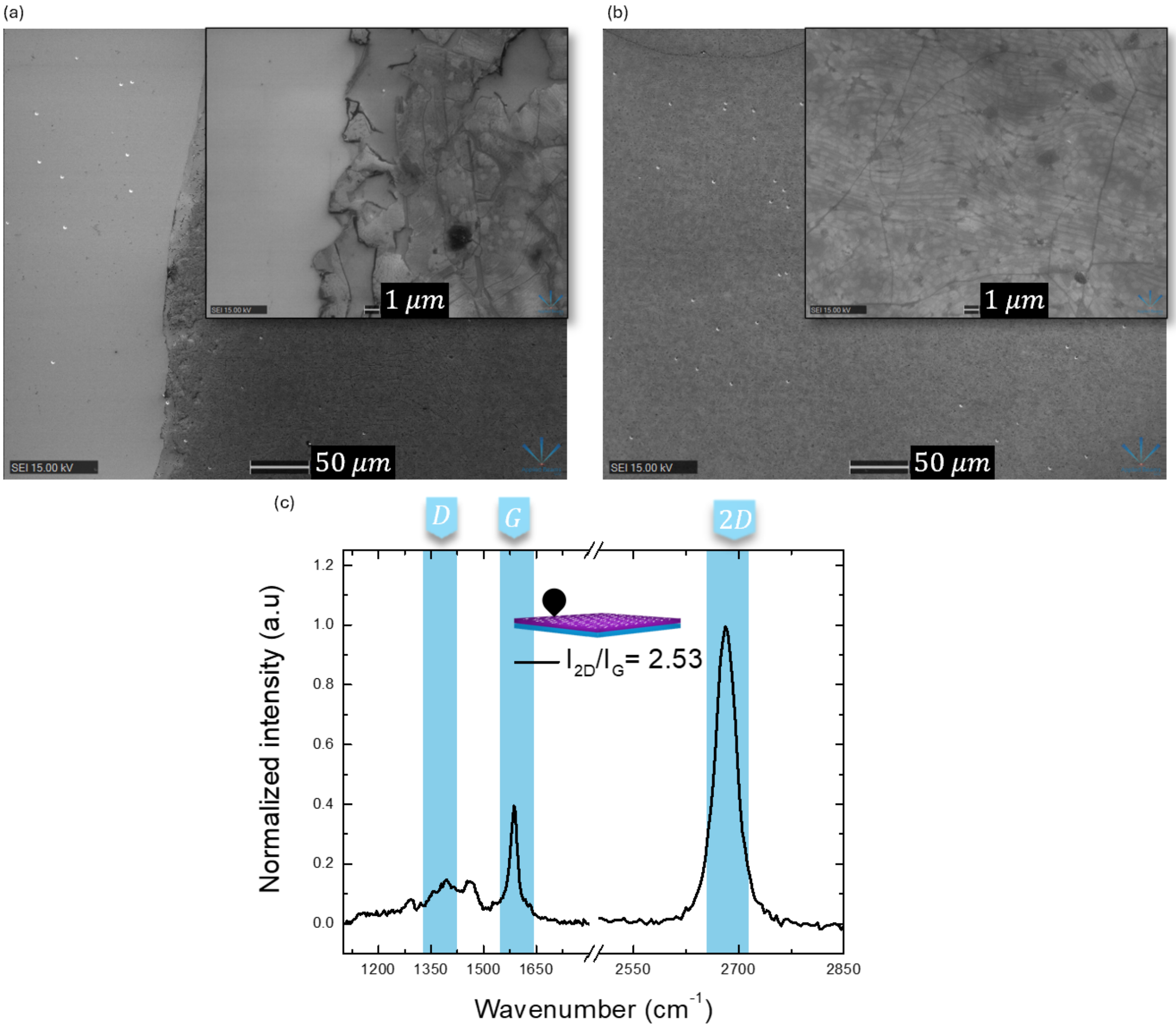

Figure 18: The SEM image showing the GaN/Al_2O_3 substrate with a wet transferred graphene layer. (a) Shows areas with and without graphene, with an inset containing a zoomed image. (b) Depicts the region in the middle of the transferred graphene with an inset containing a zoomed image. (c) Raman shift spectrum of graphene transferred with wet method.

From Figure 18 (a), a clear identification of the substrate surface with graphene could be made, as the area with graphene appeared darker due to higher conductivity. Furthermore, graphene-empty areas seemed to be free of contaminants, indicating the possibility of using samples in epitaxial growth with a MOVPE reactor. Investigating the center of the transferred graphene (see Figure 18 (b) inset), grains were visible. These grains were connected with grain boundaries, and no tearing along grain boundaries was observed. Additionally, darker spots were visible (see Figure 18 (b) inset), which could be explained by two-layer or multilayer graphene, as the graphene supplier itself presented similar images with darker spots classified as two-layered graphene [50].

In addition, the Raman shift spectrum of wet-transferred graphene was recorded to further investigate its quality (see Figure 18 (c)). The main peaks of graphene (2D at 2681 cm^{-1}, G at 1587 cm^{-1} and broad D peak in the 1312-1440 cm^{-1} range) were visible in the Raman spectrum. The intensity ratio of 2D and G peaks was greater than 2 (I_{2D}/I_G = 2.53), indicating single-layer unstrained graphene [24,51]. The defect peak D around 1350 cm^{-1} confirmed the presence of disorder-induced features such as grains and could have some structural holes. The peak was broadened due to overlap with GaN substrate peak.

SEM images of wet-transferred graphene and the visible characteristic graphene peaks in Raman spectroscopy indicated that such high-quality graphene could have been utilized for the 2D material-assisted or even remote epitaxy of GaN on graphene/GaN/Al_2O_3 substrates. Furthermore, it was evident that the graphene was monolayer, potentially enabling the substrate's atomic potential to penetrate through this type of 2D interlayer [22]. However, local defects could have resulted in pinhole-based epitaxy. Similar quality transferred graphene was further used for GaN growth.

Additionally, an alternative and novel graphene transfer method using a laminator was examined (see the transfer procedure in Subsection 2). With this transfer method was demonstrated the capability to transfer large areas of graphene [52]. Thus, making this type of transfer a perfect candidate for whole substrate-scale 2D material-assisted epitaxy. In this study, graphene was also transferred using a laminator. Initially, the surfaces of copper with graphene and the polymer used in the lamination process were visually inspected with an optical microscope and SEM (see Figure 19a).

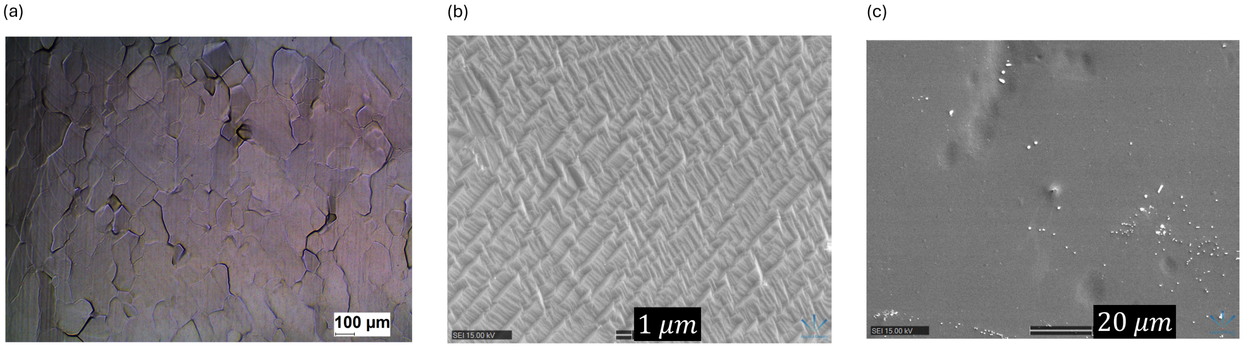

Figure 19: Inspection of graphene and PVA during various stages of transfer using a laminator. (a) Optical microscope view of graphene on a copper substrate before the transfer, where graphene was barely visible. (b) SEM image of the same graphene on a copper substrate before transfer. (c) SEM image of the PVA surface before transfer.

The micrometer-scale copper foil domains were visible with an optical microscope. SEM images (see Figure 19 (b)) revealed a more detailed surface morphology of the Cu foil, revealing a patterned type structure. Such surface morphology could influence the quality of the transferred graphene. To fully examine this transfer method, graphene on copper foils from other manufacturers should be tested. The PVA surface (see Figure 19 (c)) seemed smooth but its quality over time could degrade due to storage conditions.

With the procedure presented in Figure 16, graphene from Cu foil was laminated onto a GaN/Al_2O_3 substrate. Figure 20 shows graphene laminated onto a 2-inch wafer using PVA. The lamination area can be easily expanded for larger wafers or reduced if necessary.

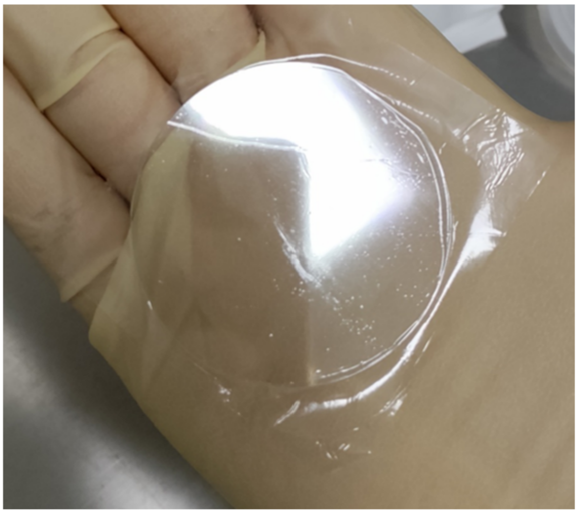

Figure 20: PVA with graphene laminated on GaN/Al_2O_3 substrate.

After lamination, the PVA must be dissolved to ensure substrate applicability in epitaxy experiments with a MOVPE reactor, as PVA leftovers could contaminate the reactor and influence growth kinetics. Figure 21 provides insights into substrate surface quality during various transfer stages.

Figure 21(a) illustrates the appearance of wrinkles on the surface after lamination, a common occurrence. In Figure 21 (b), polymer residues was visible after transfer. Raman characterization in Figure 21 (c) supported these observations with the presence of a broad D-peak around 1350 cm^{-1}. Variances in frequency and magnitude of these defects were observed among the 4 measured spots. The 2D peak at 2685 cm^{-1} and the G peak at 1581 cm^{-1} were also observed. The slight shift of the 2D peak compared to the wet transfer case could indicate that the graphene was stressed during transfer and, after the transfer, was in a stress-released state [51]. SEM examination of the substrate surface revealed torn-up dense graphene flakes. Additionally, polymer contamination was evident in areas without graphene, indicated by less conductive, lighter-colored dots, likely PVA remnants. PVA removal was achieved through rapid thermal annealing at 300°C for 6 hours (see Figure 22), although untorn graphene appeared to be also removed. EDX mapping confirmed that the darkened spots consisted of carbon, thus confirming graphene composition. Of particular interest was the intensity ratio of the 2D and G peaks, which exceeded 2, indicating monolayer graphene and being almost unaffected by the presence of ripped patches.

Such poor-quality graphene is not applicable for remote epitaxy experiments. However, 2D material-assisted growth can still be performed, as the strong covalent bonding of the whole epilayer area to the substrate should be heavily reduced due to intersections of graphene and its flakes. Thus, the growth regime is likely to be more like pin-hole assisted.

The unsatisfactory graphene transfer was likely caused by the use of hard and relatively brittle polymer or the degradation of the polymer itself. This degradation likely occurred due to prolonged

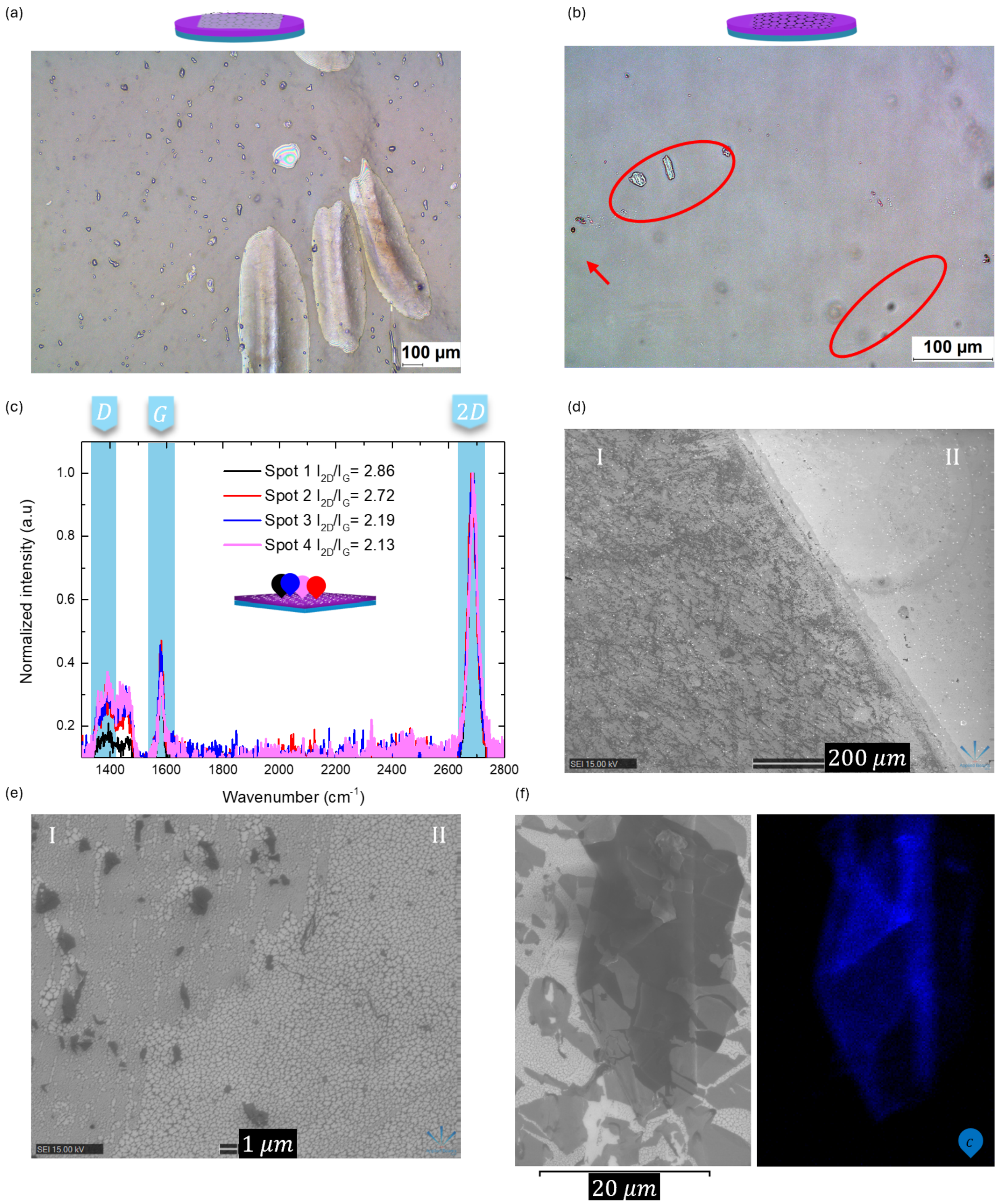

Figure 21: Inspection of the GaN/Al_2O_3 surface at various stages of transfer using a laminator. (a) Optical microscope view of PVA with graphene laminate on the GaN/Al_2O_3 substrate as shown in Figure 19. (b) Optical microscope view of the GaN/Al_2O_3 surface with graphene after prolonged PVA dissolution in water. The marked spot indicates PVA residue. (c) Raman spectra of transferred graphene using the laminator. (d, e) Images taken with SEM show the substrate surface after prolonged cleaning, where area I exhibits transferred graphene and area II shows only PVA residue. (f) The SEM image depicts a large torn graphene flake alongside its corresponding EDX carbon elemental map.

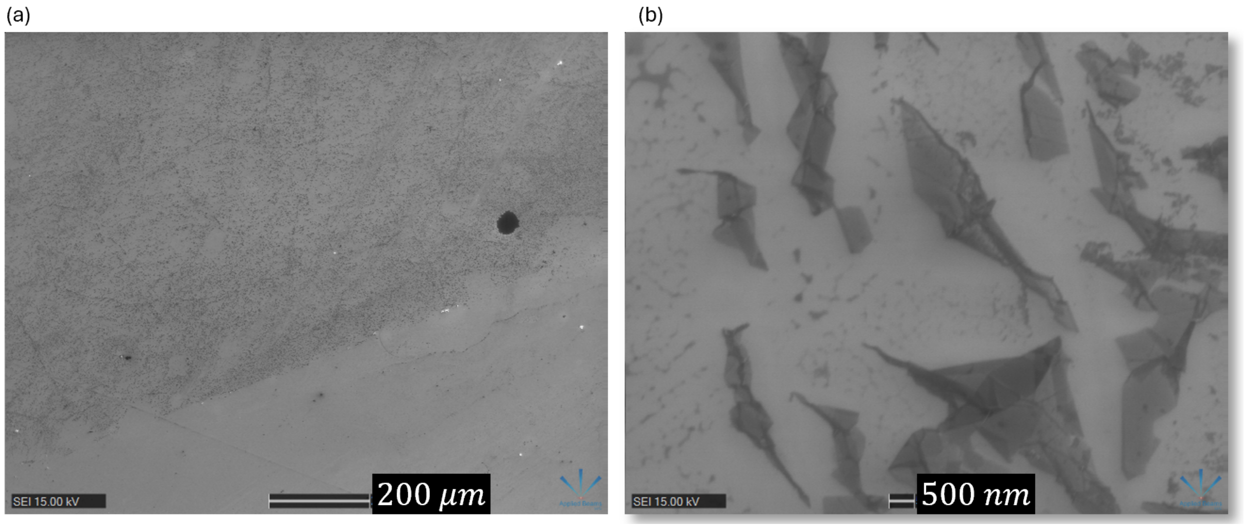

Figure 22: The SEM image depicting the GaN/Al_2O_3 substrate with transferred graphene flakes after prolonged cleaning and additional thermal annealing.

storage in a humid environment, where water absorption negatively affected the mechanical properties of the materials [53].

3.3 Stressor deposition on arbitrary substrates

On the transferred graphene, GaN was grown (see growth characteristics in following Subsection 3.4), and afterward, exfoliation was carried out. For successful exfoliation, the deposition of the stressor material was carried out. In this case, Ni was electroplated onto several surfaces and first inspected visually with SEM (see Figure 23).

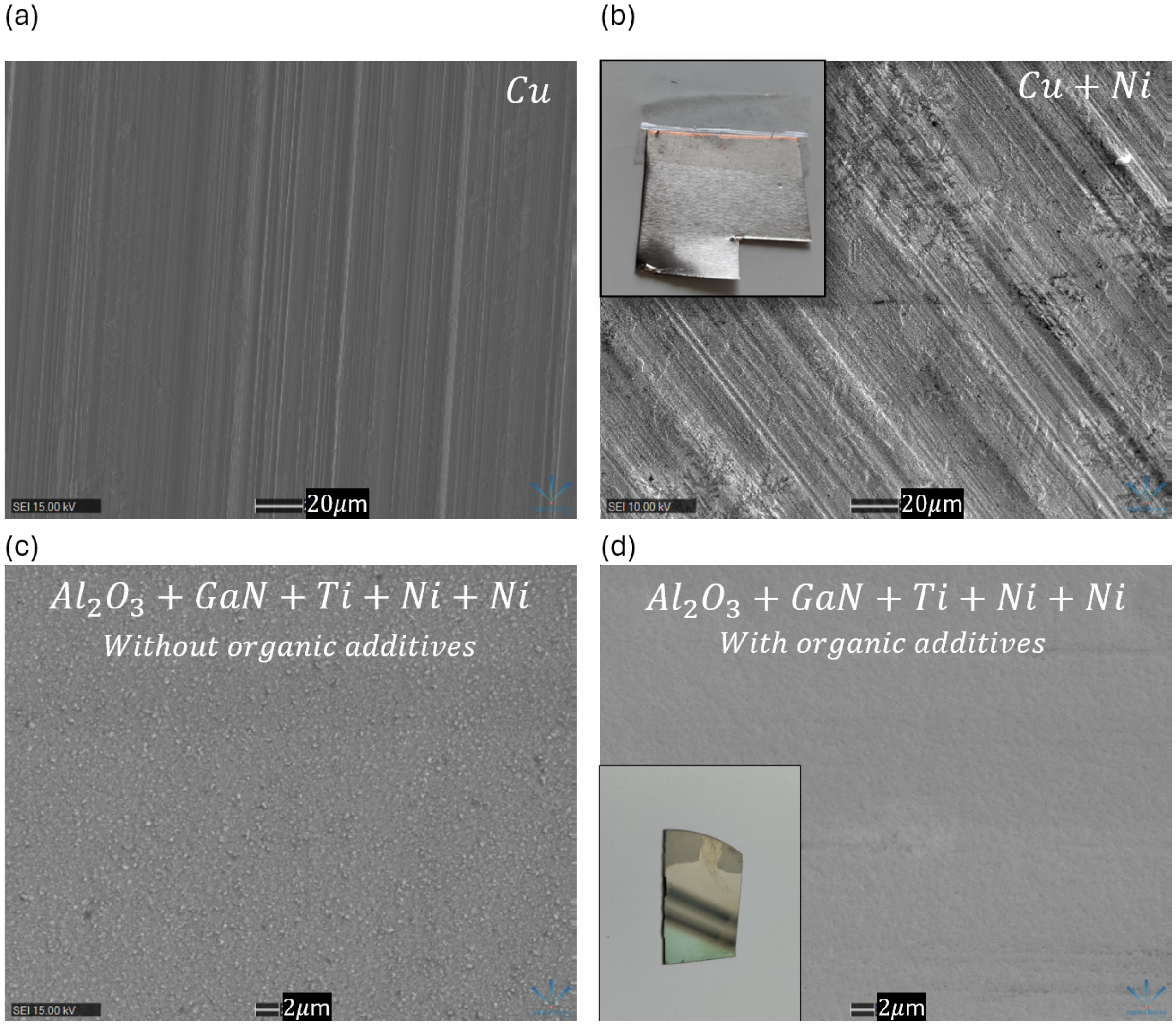

Figure 23: Images taken with SEM showing various surfaces before and after Ni stressor deposition. (a) Copper foil surface before Ni electroplating with $NiSO_4 \cdot 6H_2O + NiCl_2 \cdot 6H_2O + H_3BO_3$, and (b) after Ni electroplating. (c) Surface of Ni/Ti/GaN/Al$_2$O$_3$ after Ni electroplating with $NiSO_4 \cdot 6H_2O + NiCl_2 \cdot 6H_2O + H_3BO_3$. (d) Surface of Ni/Ti/GaN/Al$_2$O$_3$ after Ni electroplating with $NiSO_4 \cdot 6H_2O + NiCl_2 \cdot 6H_2O + H_3BO_3 + C_7H_5NO_3S + C_3H_4O$.

The initial tests were carried out on inexpensive copper foils using a solution electrolyte of $0.67MNiSO_4 \cdot 6H_2O + 0.49MNiCl_2 \cdot 6H_2O + 0.59MH_3BO_3$. The deposited metal surface appeared continuous, but the irregularities of the copper foil itself remained visible after electrodeposition (Figure 23 (b)). Further optimization was conducted using more realistic samples (GaN/Al$_2$O$_3$ substrates with deposited 50 nm Ti and 50 nm Ni, and 50 nm Ti and 50 nm Au adhesive layers), which were electroplated under similar conditions (Figure 23 (c)). The surfaces of these samples also appeared continuous but grains and imperfections were visible. In principle, such deposited layers could be used for exfoliation experiments. However, without organic brighteners, Watts-type electroplated deposits exhibit high residual stress levels and poor adhesion [32–35]. Excessively high stress levels could cause GaN to exfoliate from the graphene during electroplating. In the ideal theoretical case, only vdW forces would prevail between these layers. Thus, under high strains, GaN could snap off during electroplating or break and be lost in the electroplating jig. As a consequence, additional brighteners were used to optimize the electrolyte. The final electrolyte contained $0.67 MNiSO_4 \cdot 6H_2O + 0.49 MNiCl_2 \cdot 6H_2O + 0.59 MH_3BO_3 + 0.91 mMC_7H_5NO_3S + 0.71 mMC_3H_4O$. This type of electrolyte yielded smoother surfaces in the deposited layers (Figure 23 (d)) and was used in the following experiments.

Several GaN/Al_2O_3 substrates with deposited 50 nm Ti and 50 nm Ni adhesive layers were selected for Ni electroplating. These adhesive layers were necessary because the Ti would strongly adhere to GaN, while the Ni layer's purpose was to increase surface conductivity for Ni electrodeposition. Electroplating was conducted under several fixed conditions: a distance between electrodes of 7 cm, electrolyte pH of 4, and electrolyte temperature of 45°C, with varying current density. The samples electroplated with higher current densities than 30 mA/cm^2, lead to uncontrolled exfoliation. This was revealed as the edges of the deposited layer lifted from the substrate due to induced strains (see Figure 24). Subsequently, the lifted layers were fully exfoliated with conductive copper tape and examined with SEM.

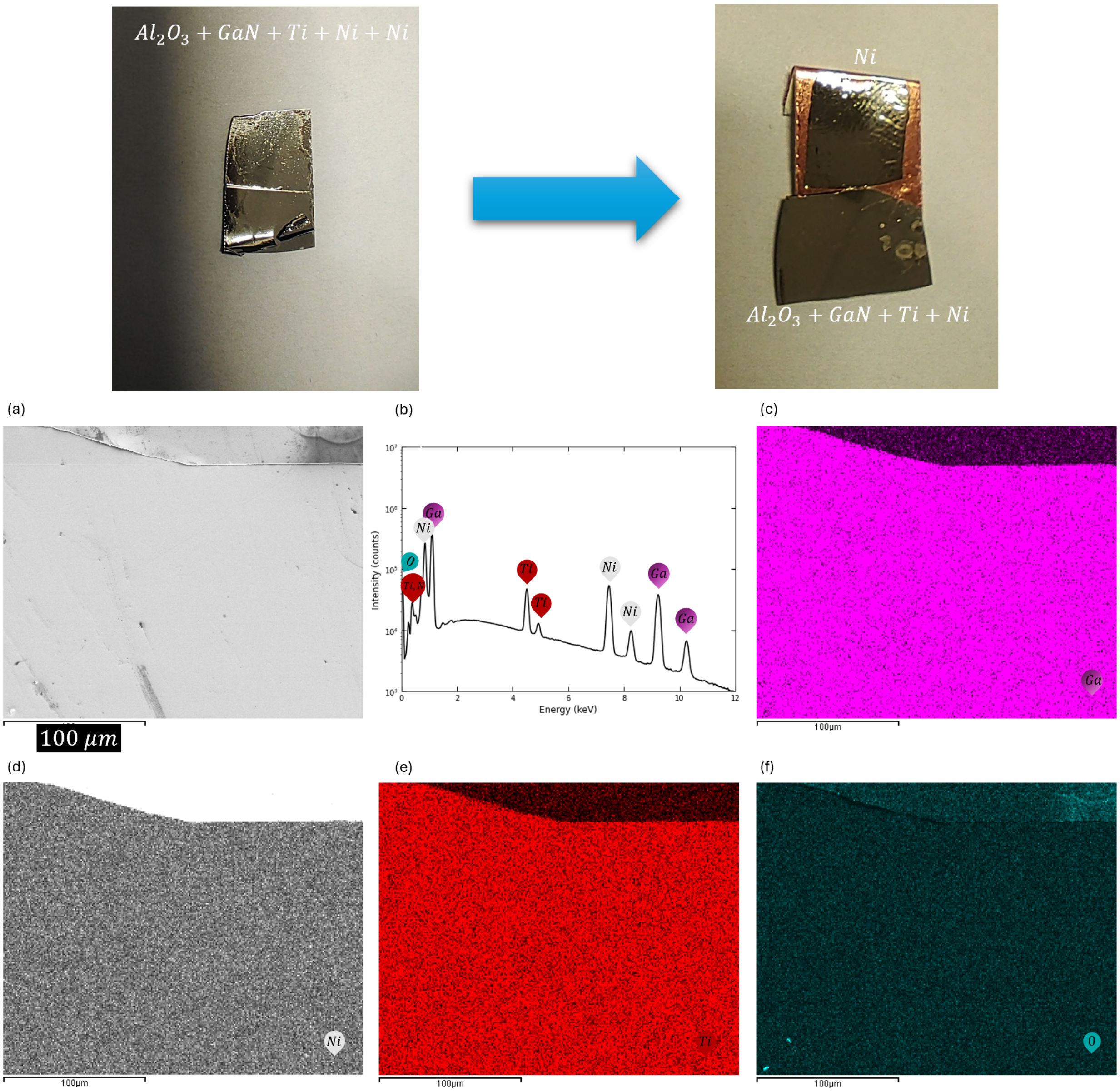

Figure 24: The upper part of the figure displays Ni/Ti/GaN/Al_2O_3 after Ni electroplating, with an arrow indicating a membrane exfoliated from this sample and the remaining substrate. Below, images depict areas of the substrate after exfoliation. (a) Shows SEM image of the zone where the unexfoliated area intersects with the exfoliated area. (b) Presents the EDX spectrum of the area seen in picture (a). (c, d, e, f) Illustrate elemental mapping of elements visible on the Ni/Ti/GaN/Al_2O_3 surface after exfoliation.

Figure 24 (a) represents a SEM image of the substrate surface after uncontrolled exfoliation. Subsequent EDX analysis of the same surface revealed Ni and Ti layers in areas from which stressors were exfoliated, as indicated by EDX maps. This suggests that only the stressor was peeled off. Additionally, oxygen was detected all over the adhesive Ni layer. Thus, it can be concluded that only the Ni stressor was exfoliated from the Ni/Ti/GaN/Al_2O_3 substrate due to high oxidation levels. The presence of surface oxides on adhesive Ni/Ti layers can interfere with the formation of strong interfacial bonds between the substrate and the electrodeposit. Oxides may act as barriers, preventing the electroplated material from making direct contact with the substrate surface, thus weakening the adhesion. Therefore, the Ti and Ni adhesive layers on GaN/Al_2O_3 substrates are not suitable for later thin GaN membrane exfoliation from graphene, as the electrodeposit won't adhere to the adhesive layers and will only exfoliate itself from the Ni/Ti/GaN/Al_2O_3 substrates. The solution to this problem could be offered by chemically etching thin oxide layers, although the etching process must also be optimized. Hence, alternative adhesive layers of 50 nm Ti and 50 nm Au were employed. Titanium would strongly adhere to GaN, while gold would prevent Ti from oxidation.

Further evaluation of electrodeposit residual stress and thickness was conducted for this concentration of electrolyte and several GaN/Al_2O_3 substrates with deposited 50 nm Ti and 50 nm Au adhesive layers.

For thickness and stress evaluation the Ti and Au adhesive layers were intentionally selected rather than Ti and Ni, as Ni tends to oxidize and causes poor adhesion (see Figure 24). Electroplating was conducted under several as fixed as possible conditions: a distance between electrodes of 7 cm, electrolyte pH of 4, and electrolyte temperature of 52°C. Various conditions were varied, such as deposition time and current density. The Ni thickness measurement using a profilometer is presented in Figure 25. The results of the Ni thickness measurement using a profilometer is presented in Figure 25 and Table 1.

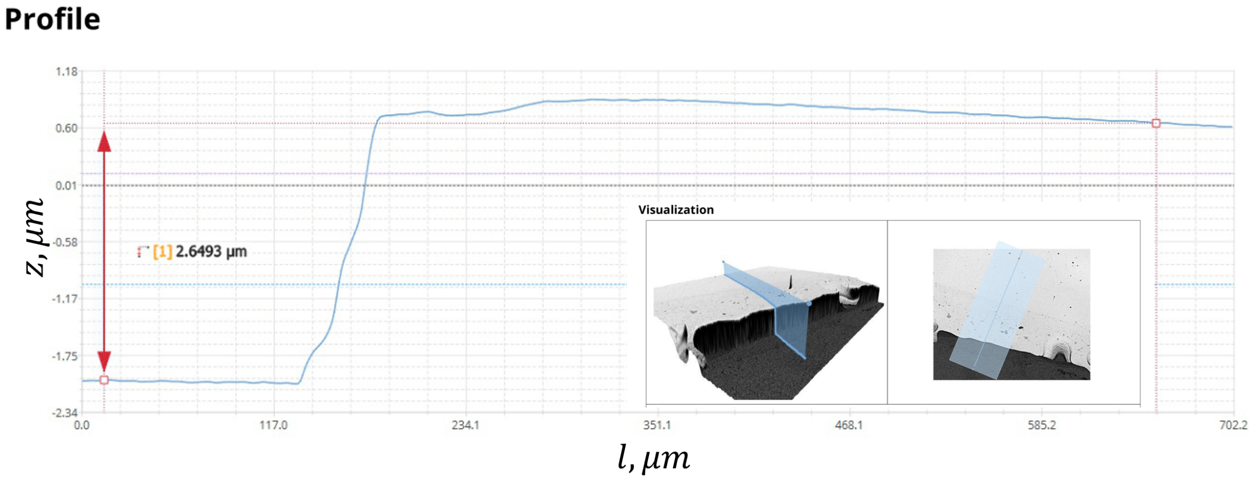

Figure 25: The electroplated nickel thickness was measured using a profilometer while varying the deposition time and current density. The image shows the measured thickness of the sample with a deposition time of 6 minutes at 25 mA/cm^2 and below is a table presenting the thicknesses of other samples measured along with their corresponding calculated values.

Table 1: The measured thicknesses of the Ni stressors with a corresponding deposition times, current densities and calculated theoretical values.

Varying conditions	Measured	Theoretical
2 min at 27 mA/cm^2	0.4 μm	1.1 μm
4 min at 25 mA/cm^2	1.5 μm	2.1 μm
4 min at 79 mA/cm^2	6.6 μm	6.4 μm
6 min at 25 mA/cm^2	2.6 μm	3.1 μm

Generally, the measured thicknesses of electroplated Ni were consistent with Faraday's Law of electrolysis (see Section 1.3.1). As the deposition time and current density increased, the amount of deposited material also increased. However, the deposited material did not perfectly match calculated thicknesses ($h = \frac{(I/S)At}{dnF}$, see Section 3). Deviations from theory occurred because the efficiency of the electroplating process was less than 100%, due to hydrogen evolution and the imperfect shape of the counter electrode, resulting in uneven thickness of electrodeposited material over the entire sample area. Furthermore, deviations of measured data from theoretical values decreased with longer deposition times, as deposition thickness became more linearly dependent on time [54]. Crystallinity and residual stresses were also measured for the same electroplated surfaces using XRD $2\theta/\psi$ scans (see Figures 26 and 27).

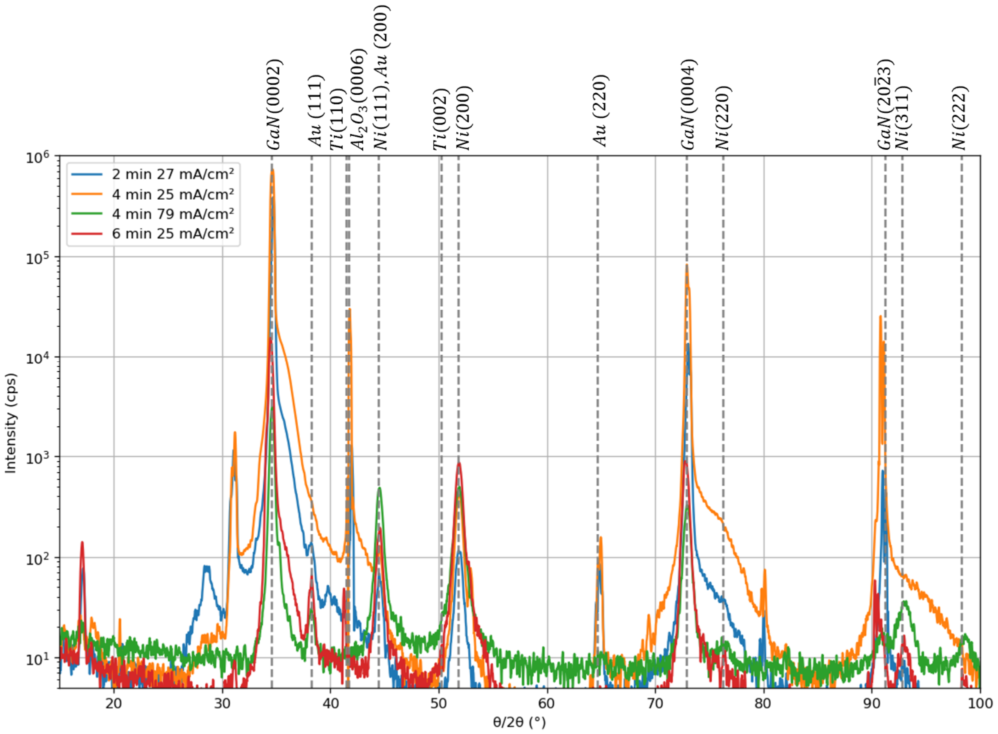

Figure 26: XRD $\theta/2\theta$ scan showing the reflection from Ni electroplated layer on an Au/Ti/GaN/Al_2O_3 substrates. Differences in electroplating conditions are denoted in the legend. The unstrained reflections were denoted from PDF Card No.: 00-055-0345, PDF Card No.: 04-013-1733, PDF Card No.: 04-010-6148, PDF Card No.: 00-042-1468 and *R.T. Downs et al.* [55].

The crystal orientation of electroplated Ni was analyzed from XRD $\theta/2\theta$ scans. The Ni crystallite orientation was identified by comparing experimental measurements with the powder diffraction file (PDF) Card No.: 04-010-6148. All measured Ni stressor layers appeared to be polycrystalline, as reflections from (111) at 44.43 °, (200) at 51.78 °, (220) at 76.26 °, (311) at 92.78 °, and (222) at 98.27 ° were visible in $\theta/2\theta$ scans. It was noticeable that the intensity of reflections from other materials greatly reduced with increasing stressor thickness, as the X-rays penetrated the underlying layers less. This effect was clearly observed in reflections from GaN (0002) planes, with a thinner Ni layer (2 minutes deposition with 27 mA/cm^2 current density), GaN reflections had a more intense signal than with a thicker layer (4 minutes deposition with 79 mA/cm^2 current density). Additionally, the reflection from the thin 50 nm Au layer on (220) planes completely vanished as the Ni layer thickened. Based on Figure 26, the Ni (111) and Ni (200) peaks were selected for stress evaluation, as these peaks were the most intense.

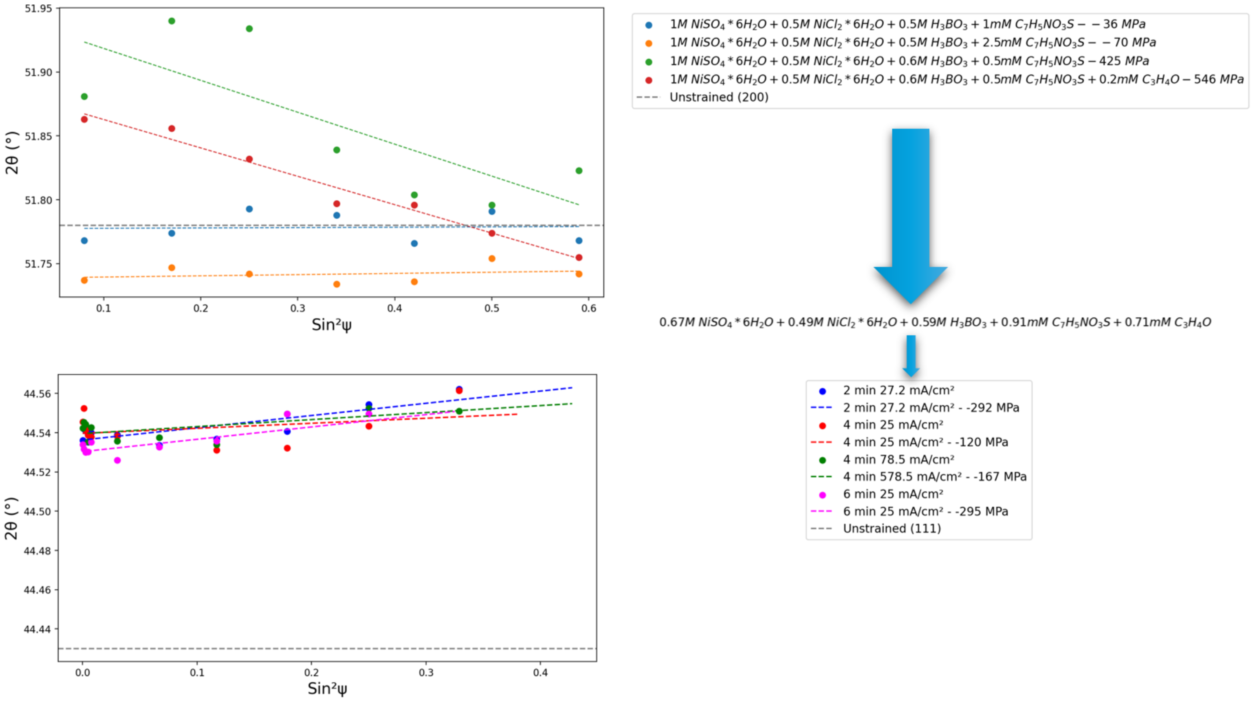

Figure 27: Results of XRD residual stress measurements depicting 2θ versus $\sin^2\psi$ of Ni (220) and (111) planes with varying thicknesses. The upper section illustrates the influence of electrolyte composition on residual stress under fixed electrodeposition conditions, while the lower section illustrates the change in residual stress due to variations in electrodeposition times and current densities with a fixed electrolyte composition. The evaluated residual stress values are provided in the legends.

Figure 27 illustrates changes in the 2θ angle or interplanar distance of (200) and (111) planes with the tilt of the sample. The deviation in 2θ observed with different samples occurs because differently oriented crystallites in polycrystalline materials experience different strains depending on their orientation in the crystal matrix. From the upper part, it was evident that the composition of the Watts electrolyte had a significant influence on residual stress. Watts electrolytes with fewer organic additives tended to form highly strained Ni deposits, with measured values of up to 546 MPa. Conversely, as the amount of organic additives increased, particularly saccharine, the stress was greatly reduced or altered. It changed the internal stress of Ni deposits from tensile stress to compressive stress. This change was mainly influenced by the alteration of crystallite size due to the presence of organic additives and sulfur from saccharine insertion into grain boundaries [32]. Additionally, the stress was evaluated for a fixed composition electrolyte with varying deposition times and current densities. It was observed that with a fixed electrolyte composition, the variation in stress was more significant than with changes in electroplating conditions. Therefore, the composition should primarily be selected for exfoliation purposes, with only minor adjustments made for electroplating conditions.

These electrolytes were further used in exfoliation experiments.

3.4 GaN membrane MOCVD growth and exfoliation

A thin GaN film was grown on GaN/Al_2O_3 via monolayer graphene transferred using the wet method (see Figure 28). The intentional growth of a small thickness GaN layer was carried out because the critical bending radius is smaller for thin films than for bulk materials (see Subsection 1.3).

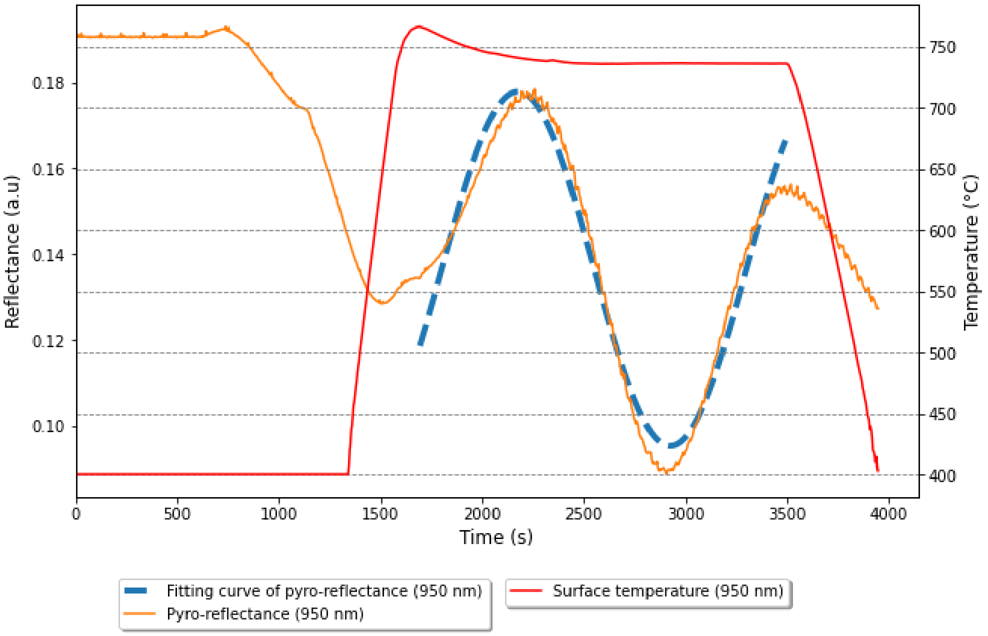

Figure 28: Growth characteristics of LT-GaN on GaN/Al_2O_3 with a graphene monolayer transferred using the wet method, including reflectance at 950 nm, surface temperature, and the fitted portion of reflectance at 950 nm for growth rate evaluation.

At first, a single-step GaN growth was conducted only at a lower temperature (700 °C) to preserve graphene, as it tends to degrade at higher temperatures [46]. However, LT-GaN is likely to exhibit poorer crystal quality compared to HT-GaN because atom migration on the substrate surface is restricted by a surface energy barrier, which is difficult to overcome at lower temperatures [56]. Thus, in this regime, GaN layers tend to grow columnarly, forming islands in preferential directions due to low surface mobility. As these islands expand in the longitudinal direction, they form a layer with domains or structural holes. Such a growth regime can be identified from the growth characteristics of LT-GaN, as the measured reflection oscillation intensity from the substrate quickly starts to drop with passing time. The reflectivity oscillations indicated that GaN layers were formed. However, the intensity decrease indicated a columnar growth regime. In this regime, GaN islands were formed during the nucleation stage. Afterward, they did not coalesce into a perfectly continuous and smooth layer but rather continued growth in islands as the vertical growth was dominant compared to other directions. From the fitted growth characteristics, the growth rate was calculated to be 0.485 $\mu m/h$, thus making the grown layer 0.243 μm thick. After such growth, a GaN layer was exfoliated with deposited Ni stressor under identical deposition conditions as discussed in the previous section. No uncontrolled exfoliation appeared, and the membrane was only exfoliated with sticky conductive copper tape. The exfoliated flexible membrane is visible in Figure 29.

Figure 29: Exfoliated flexible membrane on sticky conductive copper tape.

Afterward, the membrane and substrate after exfoliation were investigated with SEM (see Figures 30 and 38).

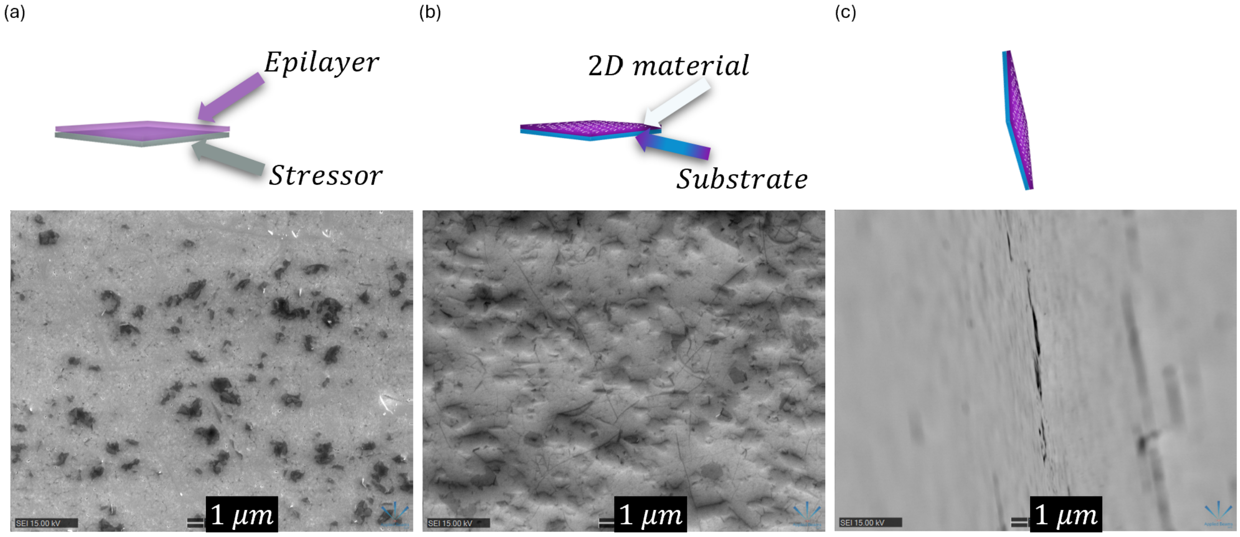

Figure 30: LT-GaN exfoliation from graphene monolayer transferred with the wet transfer method on GaN/Al_2O_3. (a) The surface of the exfoliated membrane captured with SEM. (b) The surface of the substrate after exfoliation captured with SEM. (c) The surface of the substrate after membrane exfoliation captured with SEM, rotated to 94 degrees.

Figure 30(a) shows the surface of the exfoliated membrane. This type of surface morphology was visible over the entire exfoliated area. The membrane was exfoliated from the region where graphene was transferred, covering an area of approximately 0.5 cm^2. The membrane was continuous, without significant cracks. However, it had structural holes. These holes appeared because the growth parameters influenced more profound vertical island growth than lateral growth, preventing the islands from merging into a perfectly flat layer. Figure 30 (b) displays the surface of the substrate after membrane exfoliation. On the surface, remnants of the graphene layer were visible, with similar grain boundaries as seen in Figure 18 (b), indicating that the graphene did not deteriorate during growth. Additionally, some structures were observed on top of the graphene. The most likely explanation for these areas is that they are remnants of the wetting layer of GaN. Parts of the wetting layer remained on the graphene due to the presence of pinhole-assisted epitaxy through structural holes in 2D material. In the presence of holes in the graphene, the epitaxial GaN layer would form a strong covalent bond during epitaxy and would not be exfoliated after stressor deposition. Only weakly bonded areas on top of graphene without holes were exfoliated. Figure 30 (c) shows the surface of the substrate after membrane exfoliation, rotated 94 degrees. It was evident that no large islands were left on the substrate, and the structures observed in Figure 18 (b) were most likely remnants of the wetting layer. Furthermore, the substrate and membrane were investigated with EDX measurements (see lower part of Figure 31).

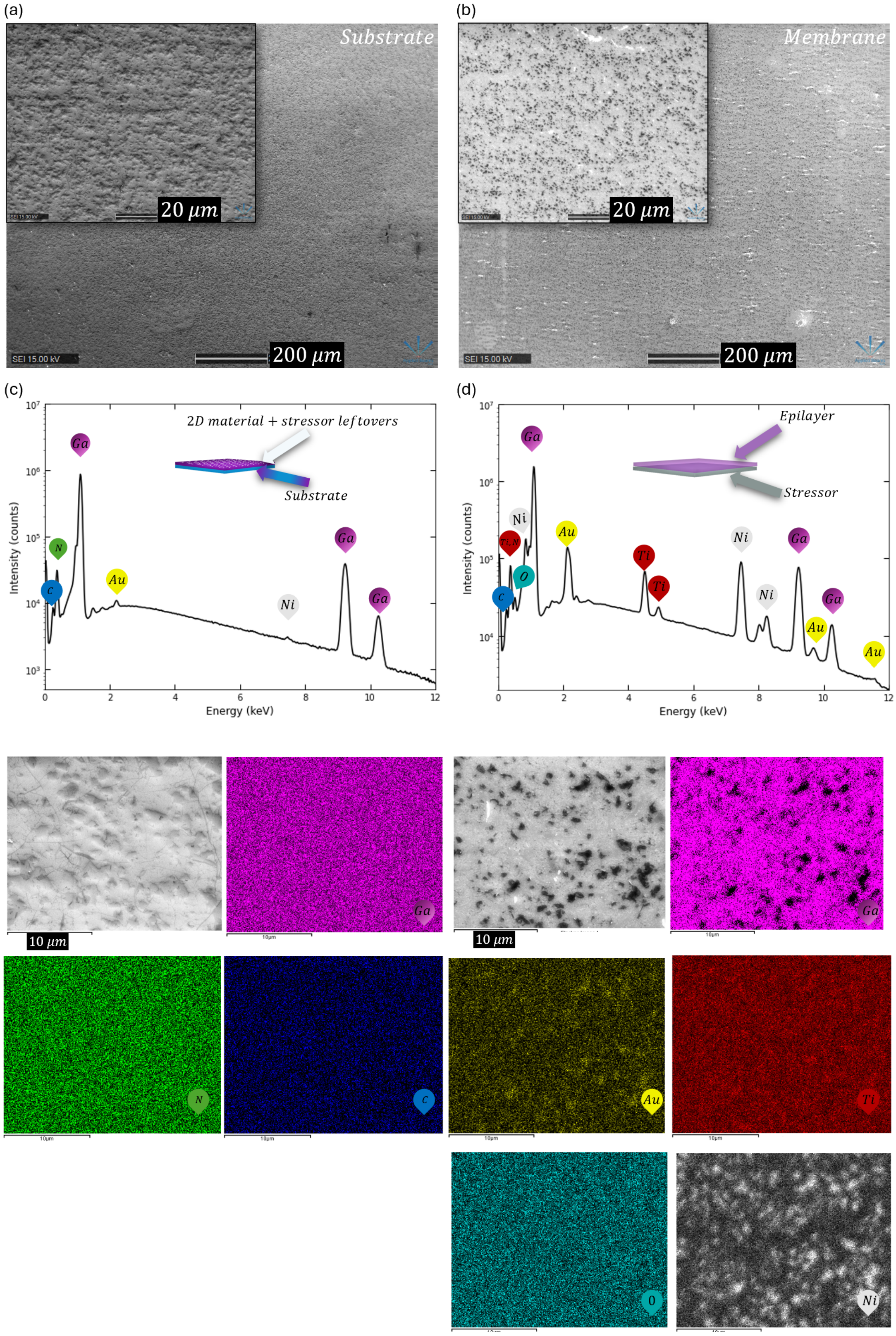

Figure 31: Exfoliated LT-GaN membrane from GaN/Al_2O_3 substrate with graphene monolayer analysis using SEM and EDX spectra. The left part of the figure corresponds to substrate analysis and the right to the exfoliated membrane. (a) The surface of the substrate after exfoliation with a zoom-in inset visible via SEM. (b) The surface of the membrane after exfoliation with a zoom-in inset visible via SEM. (c) EDX spectrum collected from the substrate surface. (d) EDX spectrum collected from the membrane surface. Below the spectra, elemental maps with corresponding SEM views are presented.

Figure 31 (c) shows the EDX spectrum collected from the substrate surface after membrane exfoliation. It was observed that some remnants of the stressor are visible in the EDX spectrum, although they appear as only local spots that were not visible in the EDX maps. The Ni and Au micro-areas from the stressor could appear on the substrate after exfoliation due to the holes in the LT-GaN layer. The darker areas on the graphene did not stand out as consisting of different elements than the GaN substrate, further justifying that these areas were GaN wetting layer remnants. Figure 31 (d) presents the EDX spectrum with the elemental maps collected from the exfoliated membrane. The exfoliated membrane consisted of GaN on the stressor layers. The larger, lighter-colored areas visible with SEM were GaN, while the darker spots were holes in the GaN through which the signal from the stressor was visible. These findings indicate that a large area membrane can be exfoliated from graphene, however, the low-temperature growth parameters must be optimized to produce high-crystalline quality layers without structural holes. Furthermore, the quality of graphene must be improved as nucleation through graphene discontinuities was observed.

Additionally, the exfoliated membrane was analyzed with cathodoluminescence, which comes from excitation with an electron beam (see Figure 32).

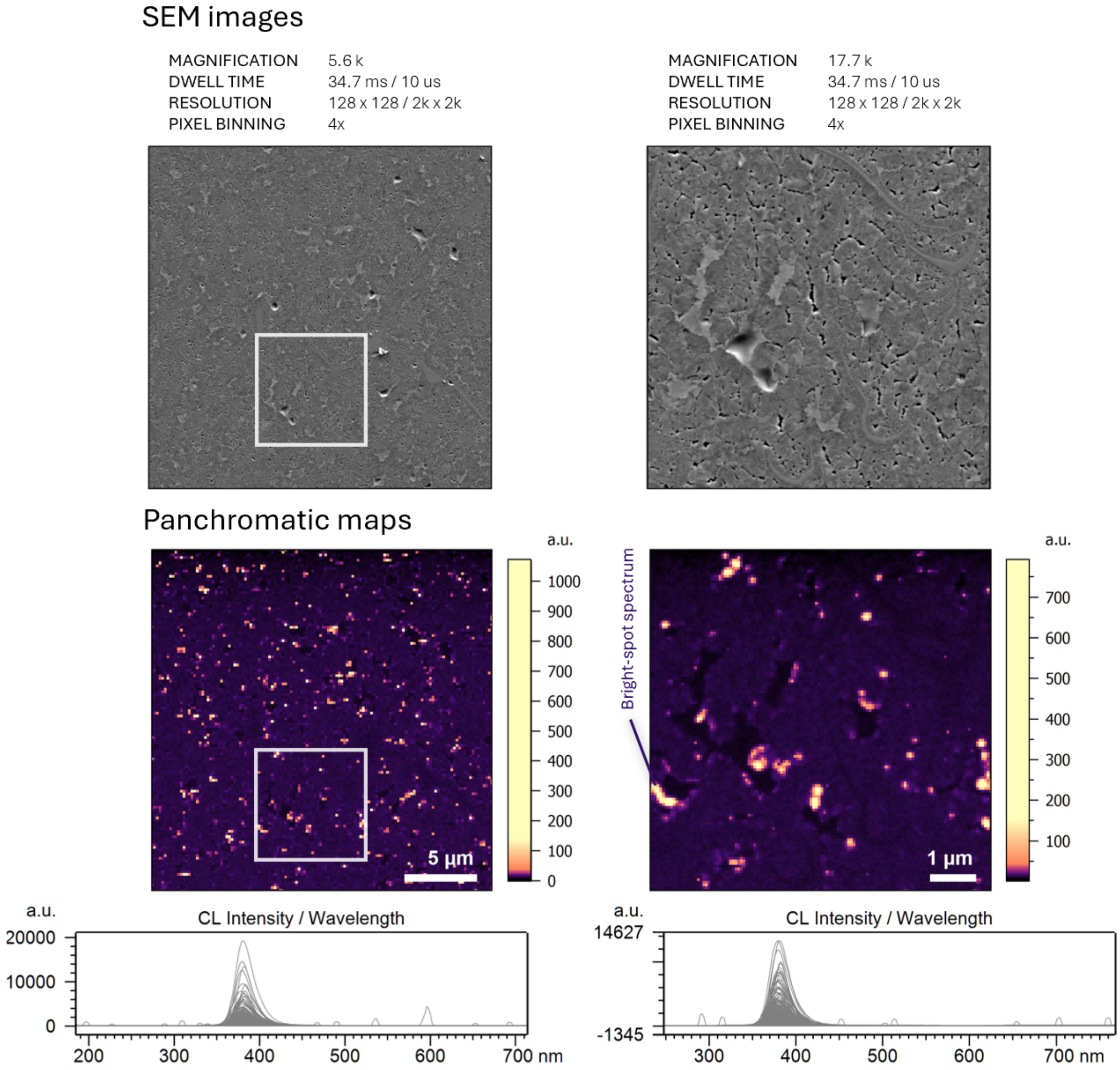

Figure 32: Upper part depicts secondary electron images in greyscale of the same LT-GaN membrane areas at increasing magnification (from left to right). The lower part depicts the spatial distribution of panchromatic cathodoluminescence intensity presented in color.

Cathodoluminescence results indicated emission from GaN at a peak value of 380 nm, corresponding to roughly 3.26 eV. A red shift was observable compared with the commonly defined 3.4 eV UV band edge emission. One possible cause is crystalline orientation distortions. It is known that crystalline orientation distortions cause effective bandgap dispersion and thus create lateral potential fluctuations. Vacancies, impurities, dangling bonds, strain, and structural defects all introduce these fluctuations [57]. As the material here is most likely not purely single crystalline, the red shift in luminescence can arise.

Another interesting observation was that the membrane exhibited spots with two orders of magnitude more intense cathodoluminescence intensities compared to the entire membrane (see Figure 40) in areas of hundreds of nanometers. The true nature of these intense spots is unclear. However, two hypotheses are likely. The first suggests that the more intense spots were nucleation sites created via remote epitaxy with specified crystal orientation. However, these islands were overgrown by other islands due to unoptimized growth conditions. The second hypothesis suggests that the more intense spots were created through holes in graphene and exhibited similar qualities as high-quality GaN substrate. As in the first hypothesis, these islands were also overgrown by more dominant islands.

Exfoliation experiments were also conducted on the areas of the substrate where graphene had not been transferred (see Figure 33). The measured results indicated that LT-GaN wasn't exfoliated from the growth substrate, as the EDX spectrum of the exfoliated structure in Figure 33 (d) shows that only the metal layers were lifted off. Additionally, metal residue was visible on the surface of the substrate. This suggested that a graphene interlayer was necessary to facilitate exfoliation. In the presence of graphene, even with structural holes, adhesion was significantly reduced because the degree of covalent bonds between the epilayer and substrate was decreased.

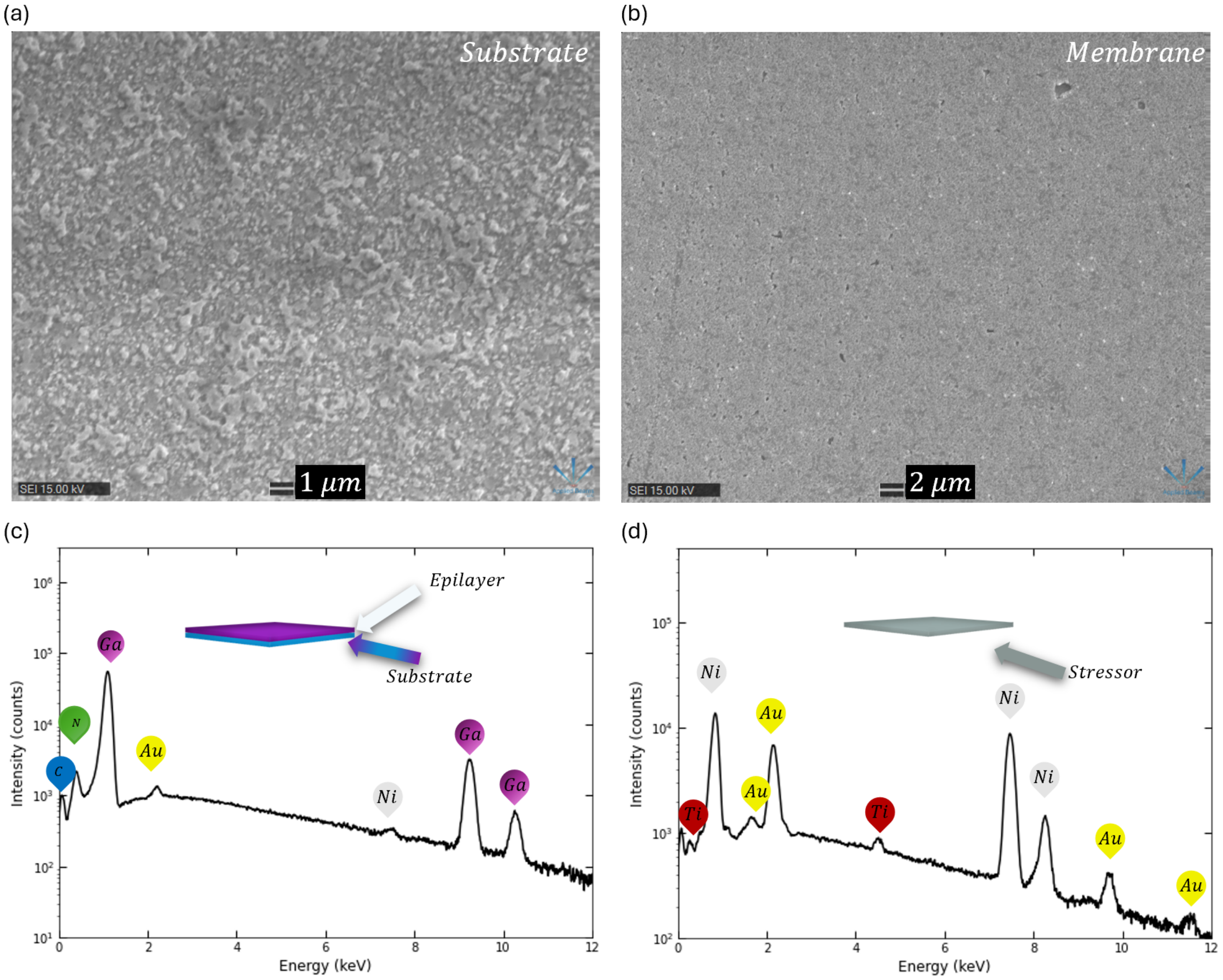

Figure 33: Exfoliated stressor layers after LT-GaN growth on GaN/Al_2O_3 substrate, where graphene was not transferred, analyzed using SEM and EDX spectra. The left part of the figure corresponds to the substrate and the right to the exfoliated layers. (a) The surface of the substrate after exfoliation visible via SEM. (b) The surface of the stressor visible via SEM. (c) EDX spectrum collected from the substrate surface. (d) EDX spectrum collected from the surface of the exfoliated layers.

A high-temperature step was added as the LT-GaN was exfoliated after a single-step growth conducted at 700 °C for 30 minutes. A two-step growth recipe was selected to preserve graphene at lower temperatures initially and then gradually increase the temperature to achieve higher crystalline quality GaN (see Figure 34).

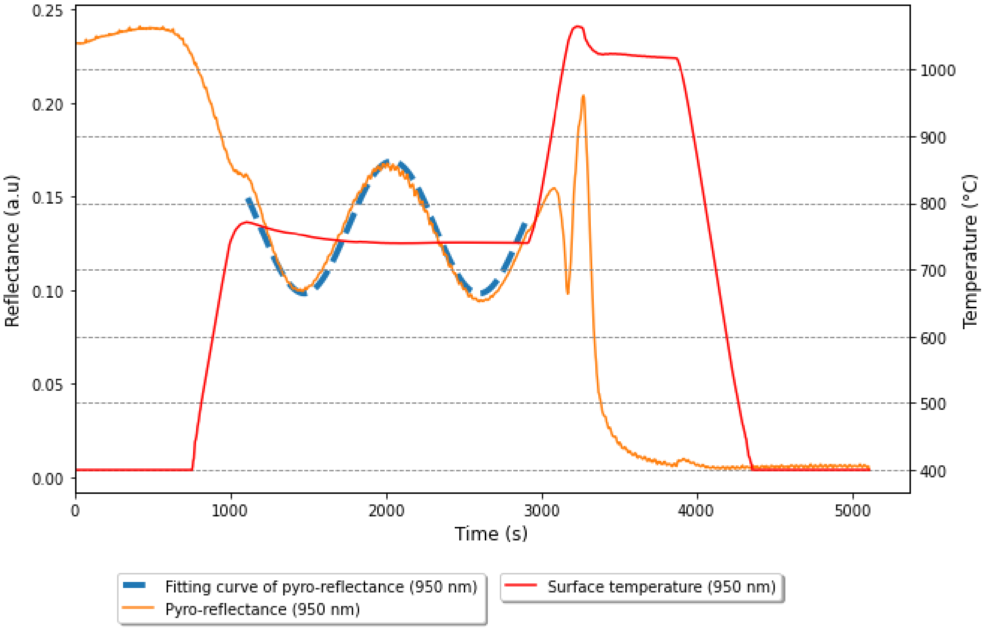

Figure 34: Growth characteristics of LT-GaN transitioning to HT-GaN on GaN/Al_2O_3 with a graphene monolayer transferred using the wet method, including reflectance at 950 nm, surface temperature, and the fitted portion of reflectance at 950 nm for growth rate evaluation.

The growth characteristics depict that after the temperature rise, the layer started rapidly coarsening. As LT-GaN layers did not fully merge and instead consisted of islands. These islands started to grow more rapidly, making the surface rougher and causing a decrease in measured reflectance. In this case, fitted growth characteristics allowed us to evaluate the growth rate of LT-GaN - 0.645 μm/h, thus making the grown layer 0.323 μm thick. The HT-GaN growth rate could not be evaluated from the presented growth characteristics as no oscillations were visible in that growth regime. After the growth, the substrate was matte. However, the area with graphene seemed a bit more transparent. The stressor was also deposited on this sample, and exfoliation experiments were conducted.

After stressor deposition, no uncontrolled exfoliation appeared. Only with copper sticky tape were the areas where graphene was not transferred exfoliated. Interestingly, the grown layers on graphene did not lift off. The exfoliated membrane and substrate were analyzed using SEM and EDX (see Figure 35).

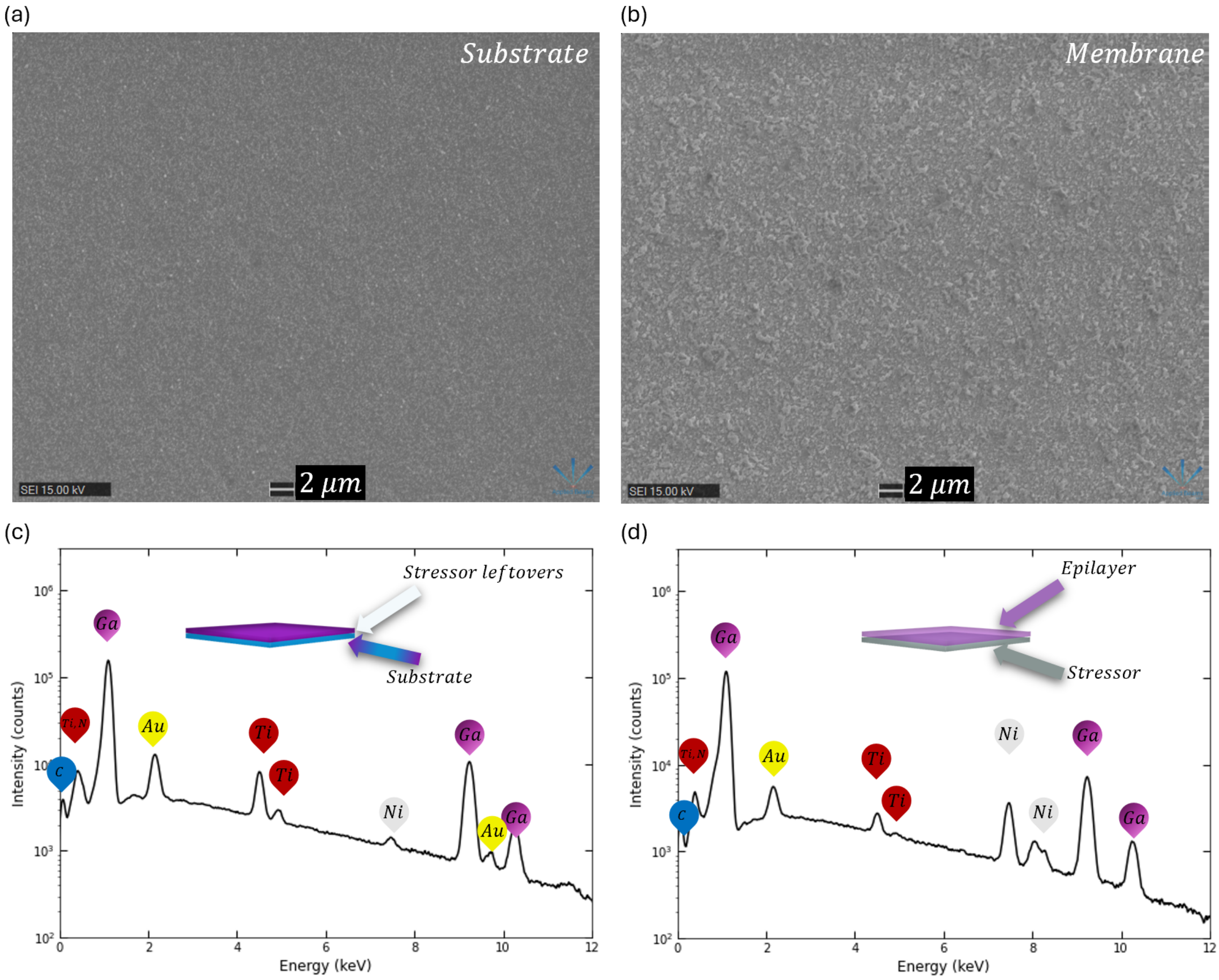

Figure 35: Exfoliated membrane after growth of LT-GaN transitioning to HT-GaN on GaN/Al_2O_3 from the area, where graphene was not transferred, analyzed using SEM and EDX spectra. The left part of the figure corresponds to the substrate and the right to the exfoliated membrane. (a) The surface of the substrate after exfoliation visible via SEM. (b) The surface of the stressor visible via SEM. (c) EDX spectrum collected from the substrate surface. (d) EDX spectrum collected from the surface of the exfoliated membrane.

In Figure 35 (c) and (d), it is visible that there was a structured and rough surface GaN on both the substrate and membrane as the metal stressor elements. Thus, some parts of GaN were exfoliated. However, the substrate 35 (a) and membrane (b) surface images indicate roughness. The explanation for these results could be that the HT-GaN was exfoliated only from LT-GaN, as in the interface between low and high-temperature grown layers where a lot of voids and structural holes. This kind of exfoliation is similar to brute force mechanical lifting shown by *H. Zhang et al.* [58].

Alternatively, LT-GaN and HT-GaN growth were conducted on graphene with torn graphene flakes as seen in Figure 21. In this case, only LT-GaN-grown GaN was exfoliated. Several growths of HT-GaN were conducted. However, there was no sign of layer lifting. This was most likely because graphene flakes burned off, and the growth was conducted using conventional epitaxy methods. The growth characteristics of the exfoliated LT-GaN are presented in Figure 36.

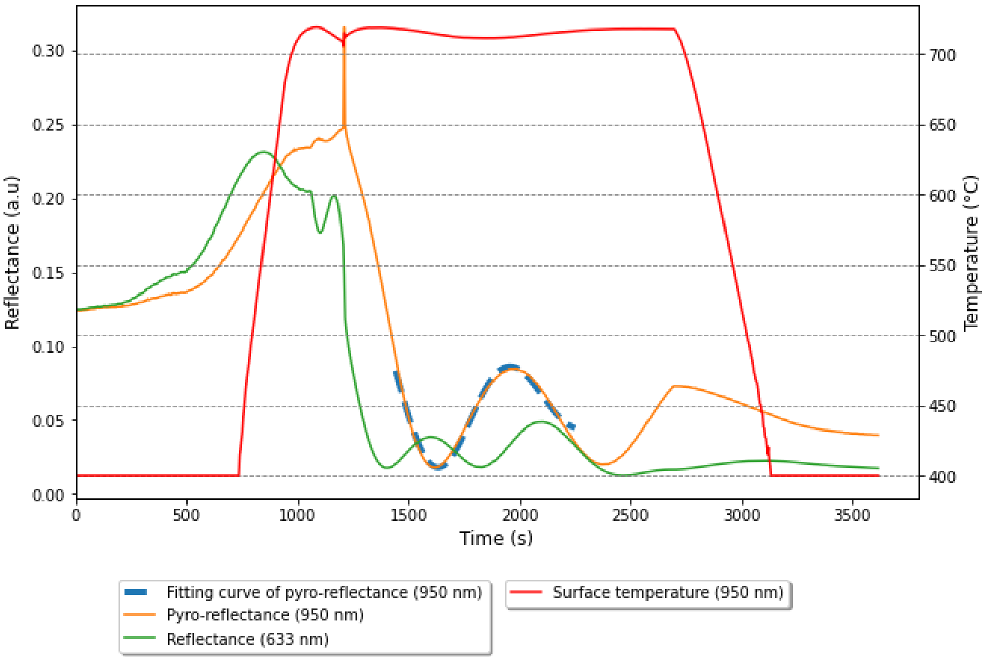

Figure 36: Growth characteristics of LT-GaN with a 150 s TMGa pre-flow on GaN/Al_2O_3 with graphene flakes transferred using a laminator, including reflectance at 950 nm and 633 nm, surface temperature, and the fitted portion of reflectance at 950 nm for growth rate evaluation.

During LT-GaN growth on graphene flakes, reflection from the surface decreased to nearly 0, most likely due to a 150 s TMGa pre-flow. However, a few oscillations appeared, indicating the formation of poor crystalline-quality GaN layers. From the fitted part of reflectance, the growth rate was evaluated - 1.123 μm/h and the grown layer thickness was 0.46 μm. Afterward, adhesion layers and Ni stressor were deposited onto GaN, and the membrane was exfoliated with copper sticky tape.

The substrate and membrane after exfoliation were investigated via SEM (see Figures 37 and 38).

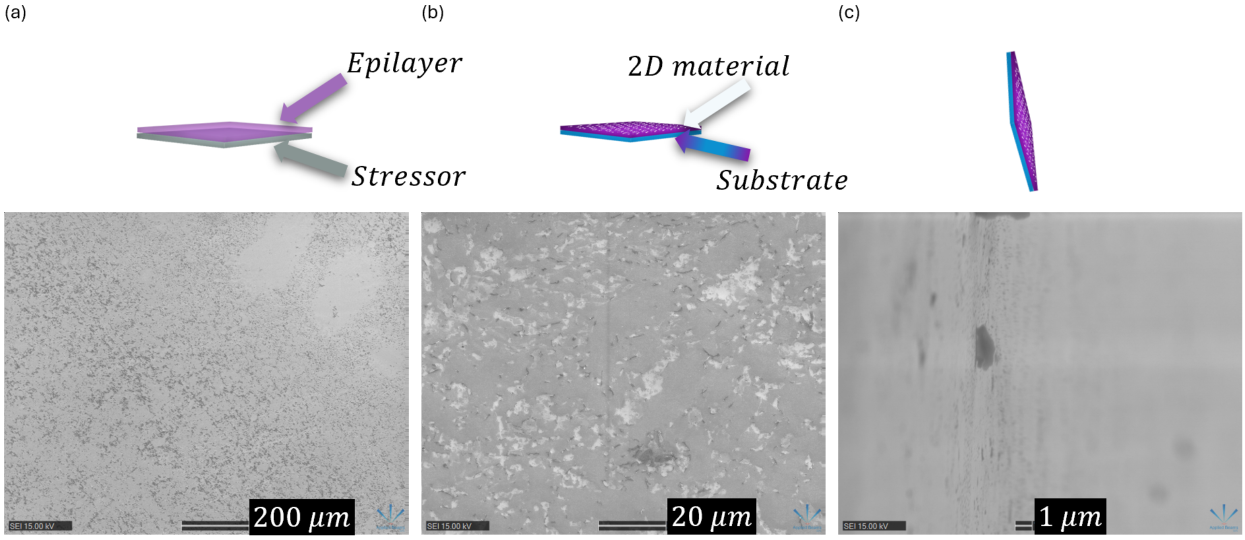

Figure 37: LT-GaN exfoliation from graphene flakes transferred with a laminator on GaN/Al_2O_3. (a) The surface of the exfoliated membrane captured with SEM. (b) The surface of the substrate after exfoliation captured with SEM. (c) The surface of the substrate after membrane exfoliation captured with SEM, rotated to 94 degrees.

SEM-taken images of the exfoliated membrane showed structural holes in the whole exfoliated area, similar to the membrane exfoliated from graphene transferred with the wet method. These holes were the result of the LT-GaN growth regime, as the grown layers were relatively porous. The substrate surface seen in Figure 37 (b) and (c) had less conductive, lighter-colored areas that were likely wetting layer leftovers after exfoliation and small, more conductive nanostripes, which were likely leftovers of graphene. Further, this hypothesis was investigated with EDX measurements (see Figure 38).

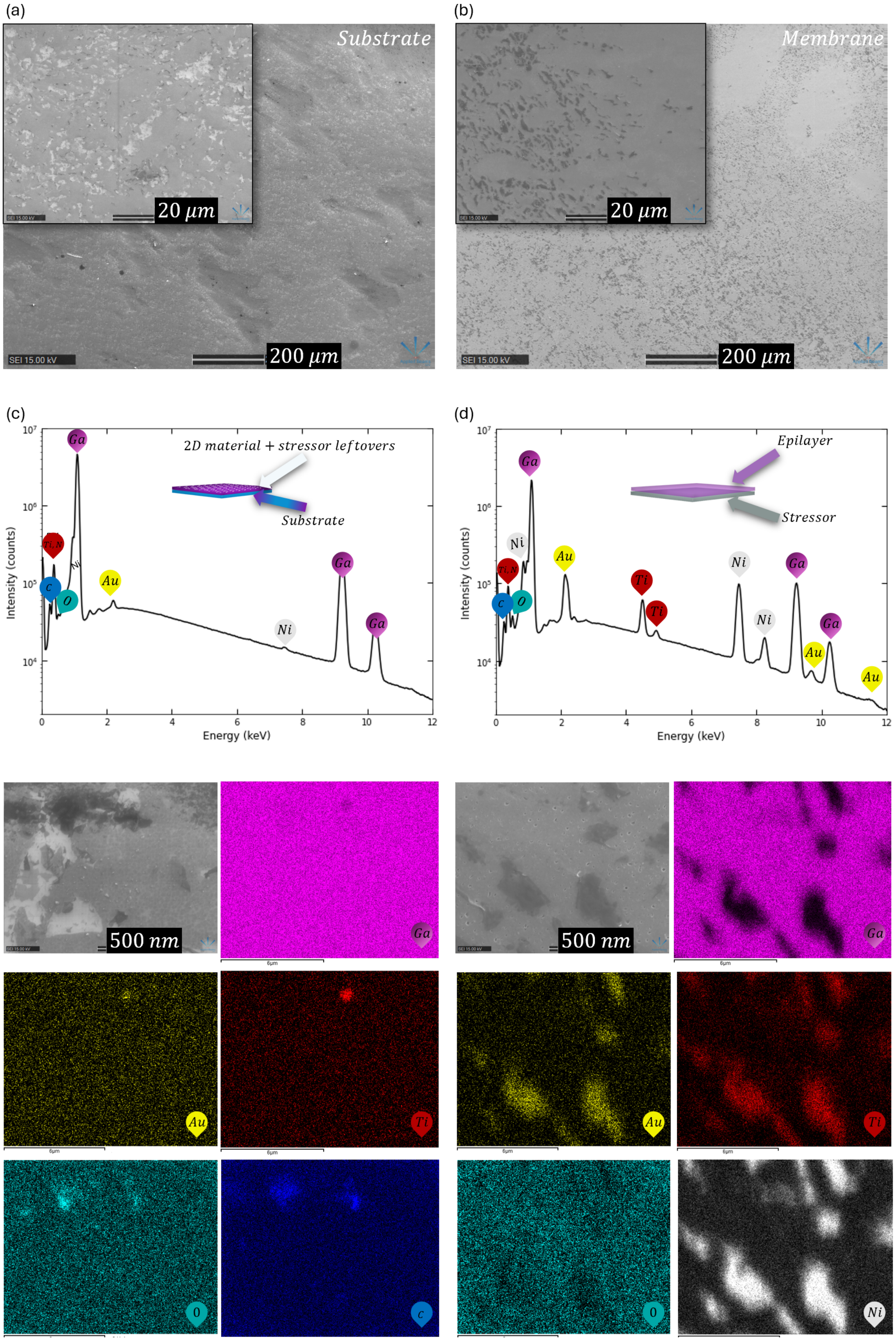

Figure 38: Exfoliated LT-GaN membrane from GaN/Al$_2$O$_3$ substrate with graphene flakes analysis using SEM and EDX spectra. The left part of the figure corresponds to substrate analysis and the right to the exfoliated membrane. (a) The surface of the substrate after exfoliation with a zoom-in inset visible via SEM. (b) The surface of the membrane after exfoliation with a zoom-in inset visible via SEM. (c) EDX spectrum collected from the substrate surface. (d) EDX spectrum collected from the membrane surface. Below the spectra, five elemental maps with corresponding SEM views are presented.

It was evident that there was GaN on both the substrate and membrane as the metal stressor elements. The lighter gray areas on the substrate surface were not distinct from the GaN substrate, indicating their composition as GaN. Noting that different contrasts indicate different conductivity levels. The light gray areas were LT-GaN wetting layer leftovers as LT-GaN would have lower conductivity than the GaN substrate because the substrate had a rather good quality (see Figure 17).

The darker nanometer-scale stripes were not identified as no specific features in element maps were found. In case these stripes were graphene leftovers, it would be hard to see them in elemental maps as the GaN substrate layer and LT-GaN had a lot of carbon impurities due to the nature of MOPVE growth. As previously mentioned, the exfoliated membrane had structural holes in GaN due to unoptimized GaN growth. However, a large area of GaN was exfoliated and further examined with cathodoluminescence (see Figure 39).

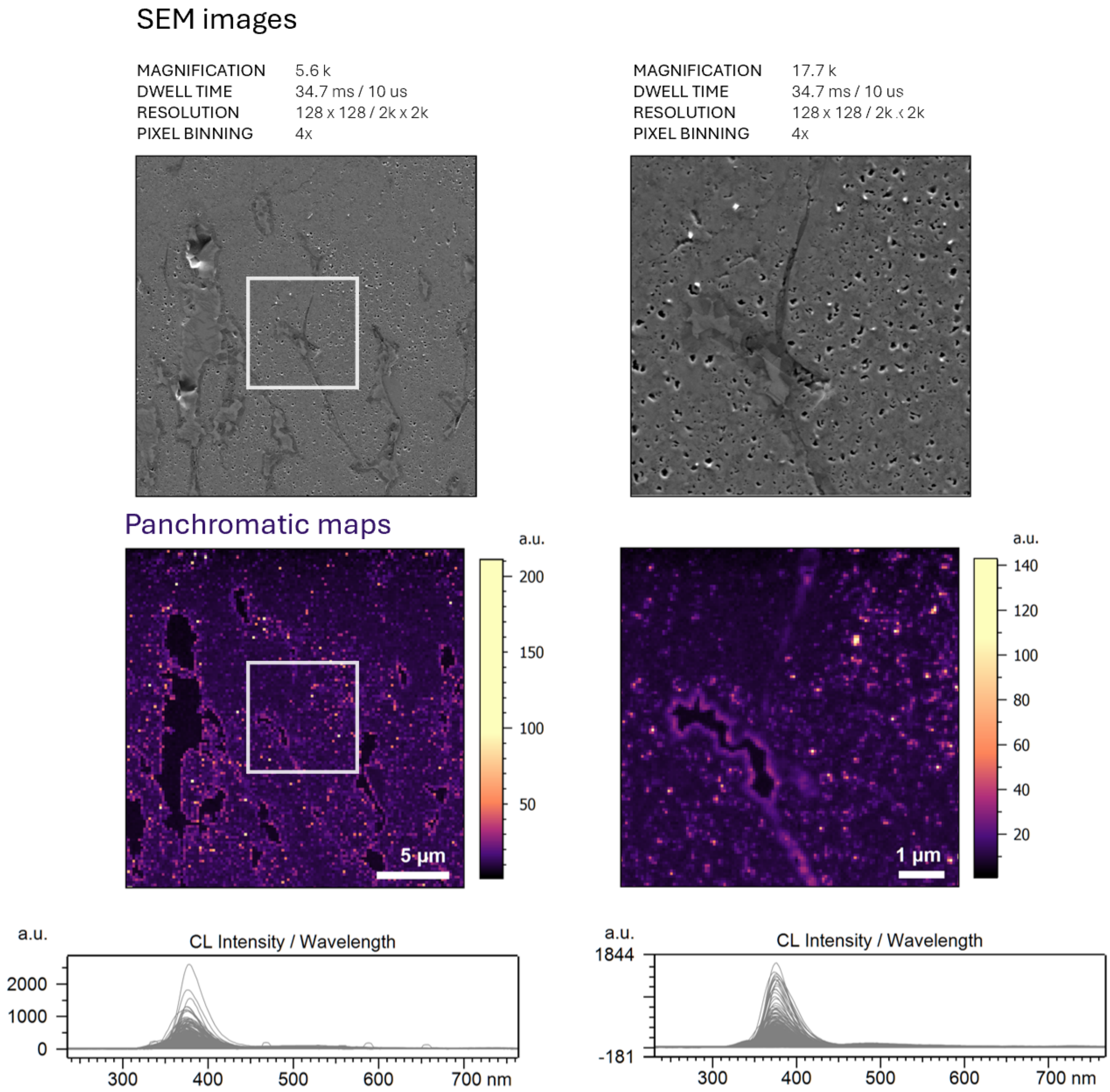

Figure 39: The upper part shows secondary electron images in grayscale of the LT-GaN membrane exfoliated from the substrate, with graphene transferred with a laminator, at increasing magnification from left to right. The lower part illustrates the spatial distribution of panchromatic cathodoluminescence intensity presented in color.

The results observed in Figure 39 resemble those from LT-GaN membranes exfoliated from the substrate, with graphene transferred using the wet method. Additionally, higher intensity spots were observed in the panchromatic maps. The origin of these spots should be the same as those described previously and should not be correlated with an escape mechanism from porous surfaces, as the more intense spots do not perfectly match hole positions.

Furthermore, membranes exfoliated from graphene transferred with a laminator exhibited lower density and smaller sizes of brighter spots. This feature could indicate that the remote regime was not as dominant as onto continuous graphene transferred with the wet method. However, this hypothesis must be further explored. Additionally, darker spots on the membranes were observed with electron images that were absent in the other exfoliated membrane. These spots highly resemble the ripped graphene flakes. Thus, these flakes could be ingrown into the layer or at least highly modify the epilayer area near them.

Further, the cathodoluminescence intensities of both membranes were compared in Figure 40.

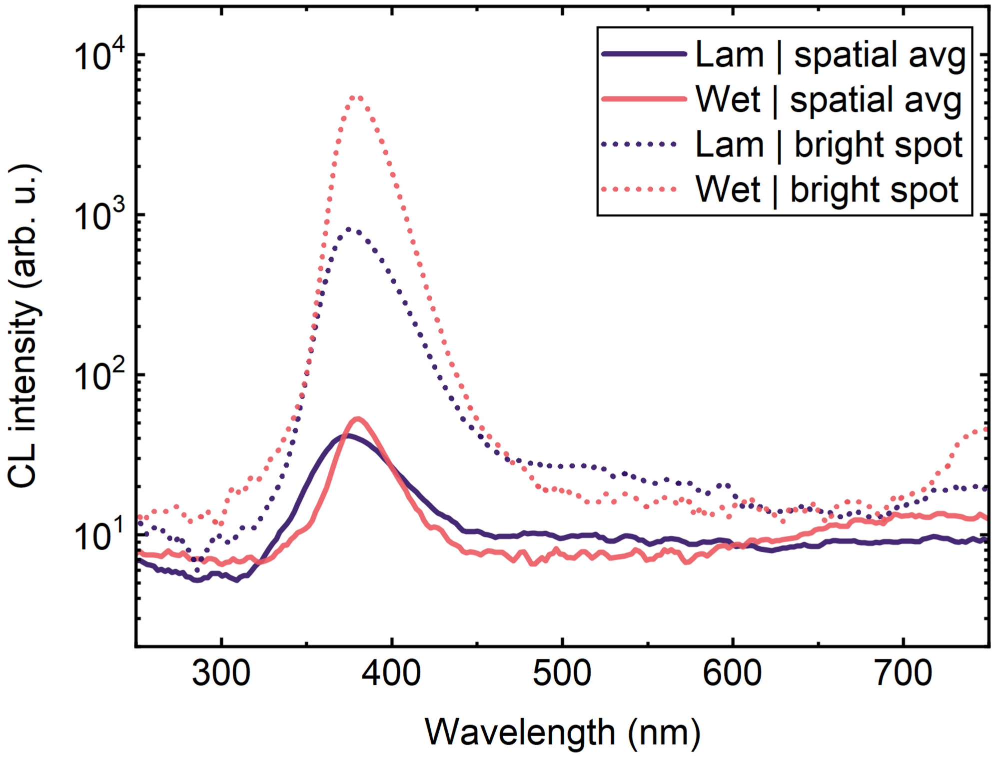

Figure 40: Cathodoluminescence spectra recorded from membranes exfoliated from graphene transferred using wet method (Wet) and laminator (Lam).

It is evident that in both membranes, the spatial average of cathodoluminescence and the local bright spot intensity differ significantly. The spot intensity is almost an order of magnitude more significant in the membrane exfoliated from wetly transferred graphene than in the other membrane, further suggesting that the remote epitaxy regime might be more profound due to better quality graphene.

In summary of all results, the 2D material interlayer, precisely graphene, is useful in thin inorganic layer lift-off procedures as it reduces the adhesion between the substrate and epilayer. Furthermore, the quality of graphene also influences lift-off. As epilayers are weakly bonded to the substrate, the electroplated stressor should not provide large stress, and additionally, it should strongly adhere to the adhesion layers. For good adhesion, unoxygenized surfaces must be selected. With graphene and Ni stressor, large epitaxial thin films of GaN can be exfoliated. However, the growth process must be optimized to achieve better quality GaN. Also, the large area graphene transfer with a laminator must be further explored and optimized to reduce the ripping of the graphene. Reducing the ripping of the graphene could be achieved by using a different lamination polymer or employing a laminator that applies less compression.

Conclusions

1. Raman spectra studies prove that monolayer graphene was transferred using wet and laminator methods.
2. SEM studies revealed that wet transfer leads to a continuous graphene layer, whereas the examined laminator method provides graphene flake morphology, which is not suitable for remote epitaxy experiments.
3. XRD analysis revealed that the residual stress in the Ni stressor strongly depends on the chemical composition of the electrolyte, while layers of different thicknesses exhibit similar stress values.
4. The oxidation of initially evaporated adhesive Ni leads to the spontaneous delamination of the electroplated Ni stressor. Replacing the Ni interlayer with Au eliminates oxidation and enhances the adhesion of the electroplated Ni stressor.
5. Graphene interlayer enables exfoliation of flexible low-temperature GaN thin epitaxial films using Ni stressor as the vdW coupling reduces adhesion between substrate and epilayer.

References

[1] T. Someya, Y. Kato, T. Sekitani, *et al.*, Conformable, flexible, large-area networks of pressure and thermal sensors with organic transistor active matrixes, *Proceedings of the National Academy of Sciences*, 2005, **102**, 12321–12325.

[2] K. J. Yu, Z. Yan, M. Han, and J. A. Rogers, Inorganic semiconducting materials for flexible and stretchable electronics, *npj Flexible Electronics*, Sept. 2017, **1**, 1–14. Publisher: Nature Publishing Group.

[3] I. Roh, S. H. Goh, Y. Meng, *et al.*, Applications of remote epitaxy and van der Waals epitaxy, *Nano Convergence*, Apr. 2023, **10**, 20.

[4] N. Yulianto, G. T. M. Kadja, S. Bornemann, *et al.*, Ultrashort Pulse Laser Lift-Off Processing of InGaN/GaN Light-Emitting Diode Chips, *ACS Applied Electronic Materials*, Feb. 2021, **3**, 778–788. Publisher: American Chemical Society.

[5] C. S. Chang, K. S. Kim, B.-I. Park, *et al.*, Remote epitaxial interaction through graphene, *Science Advances*, Oct. 2023, **9**, eadj5379. Publisher: American Association for the Advancement of Science.

[6] J. Shin, H. Kim, S. Sundaram, *et al.*, Vertical full-colour micro-leds via 2d materials-based layer transfer, *Nature*, 2023, **614**, 81–87.

[7] M. Shur, A. Bykhovski, and R. Gaska, Pyroelectric and piezoelectric properties of gan-based materials, *MRS Online Proceedings Library (OPL)*, 1998, **537**, G1–6.

[8] W. C. Johnson, J. B. Parson, and M. C. Crew, Nitrogen Compounds of Gallium. III, *The Journal of Physical Chemistry*, Oct. 1932, **36**, 2651–2654. Publisher: American Chemical Society.

[9] F. Roccaforte and M. Leszczynski, Introduction to Gallium Nitride Properties and Applications, in *Nitride Semiconductor Technology*, 1–39, John Wiley & Sons, Ltd, 2020. Section: 1 _eprint: https://onlinelibrary.wiley.com/doi/pdf/10.1002/9783527825264.ch1.

[10] O. Malyk, Charge carrier mobility in gallium nitride, *Diamond and Related Materials*, Mar. 2012, **23**, 23–27.

[11] T. Wonglakhon and D. Zahn, Interaction Potentials for modelling GaN precipitation and solid state polymorphism, *Journal of Physics: Condensed Matter*, Feb. 2020, **32**.

[12] D. Ehrentraut, E. Meissner, and M. Bockowski, *Technology of gallium nitride crystal growth*, vol. 133. Springer Science & Business Media, 2010.

[13] Y. Wang, Current methods for gan synthesis and the limitations, in *Journal of Physics: Conference Series*, vol. 1676, 012002, IOP Publishing, 2020.

[14] H. Okumura, K. Balakrishnan, H. Hamaguchi, *et al.*, Analysis of mbe growth mode for gan epilayers by rheed, *Journal of crystal growth*, 1998, **189**, 364–369.

[15] K. Badokas, *Remote epitaxy of GaN via graphene on GaN/sapphire templates by MOVPE*. PhD Thesis, Vilniaus universitetas., 2022.

[16] S. Hu, S. Liu, Z. Zhang, H. Yan, Z. Gan, and H. Fang, A novel MOCVD reactor for growth of high-quality GaN-related LED layers, *Journal of Crystal Growth*, Apr. 2015, **415**, 72–77.

[17] L. Liu and J. H. Edgar, Substrates for gallium nitride epitaxy, *Materials Science and Engineering: R: Reports*, 2002, **37**, 61–127.

[18] A. R. Urade, I. Lahiri, and K. S. Suresh, Graphene Properties, Synthesis and Applications: A Review, *JOM*, Mar. 2023, **75**, 614–630.

[19] C. J. Shearer, A. D. Slattery, A. J. Stapleton, J. G. Shapter, and C. T. Gibson, Accurate thickness measurement of graphene, *Nanotechnology*, Feb. 2016, **27**, 125704. Publisher: IOP Publishing.

[20] K. Nagashio, T. Nishimura, K. Kita, and A. Toriumi, Mobility Variations in Mono- and Multi-Layer Graphene Films, *Applied Physics Express*, Jan. 2009, **2**, 025003.

[21] S.-H. Bae, H. Kum, W. Kong, *et al.*, Integration of bulk materials with two-dimensional materials for physical coupling and applications, *Nature Materials*, June 2019, **18**, 550–560. Number: 6 Publisher: Nature Publishing Group.

[22] W. Kong, H. Li, K. Qiao, *et al.*, Polarity governs atomic interaction through two-dimensional materials, *Nature materials*, 2018, **17**, 999–1004.

[23] H.-M. Kwak, J. Kim, J.-S. Lee, *et al.*, 2D-Material-Assisted GaN Growth on GaN Template by MOCVD and Its Exfoliation Strategy, *ACS Applied Materials & Interfaces*, Dec. 2023, **15**, 59025–59036. Publisher: American Chemical Society.

[24] K. Badokas, A. Kadys, J. Mickevičius, *et al.*, Remote epitaxy of GaN via graphene on GaN/sapphire templates, *Journal of Physics D: Applied Physics*, 2021, **54**, 205103. Publisher: IOP Publishing.

[25] E. P. Randviir, D. A. C. Brownson, and C. E. Banks, A decade of graphene research: production, applications and outlook, *Materials Today*, Nov. 2014, **17**, 426–432.

[26] X. Wang, J. Choi, J. Yoo, and Y. J. Hong, Unveiling the mechanism of remote epitaxy of crystalline semiconductors on 2D materials-coated substrates, *Nano Convergence*, Aug. 2023, **10**, 40.

[27] J. Ji, H.-M. Kwak, J. Yu, *et al.*, Understanding the 2D-material and substrate interaction during epitaxial growth towards successful remote epitaxy: a review, *Nano Convergence*, Apr. 2023, **10**, 19.

[28] Y. Chen, Y. Zhang, Z. Liang, Y. Cao, Z. Han, and X. Feng, Flexible inorganic bioelectronics, *npj Flexible Electronics*, Feb. 2020, **4**, 1–20. Publisher: Nature Publishing Group.

[29] Y. D. Gamburg and G. Zangari, *Theory and Practice of Metal Electrodeposition*. New York, NY: Springer, 2011.

[30] Nickel plating handbook, 2014.

[31] S. Sengupta, A. Patra, S. Jena, K. Das, and S. Das, A Study on the Effect of Electrodeposition Parameters on the Morphology of Porous Nickel Electrodeposits, *Metallurgical and Materials Transactions A*, Mar. 2018, **49**, 920–937.

[32] Y. Li, J. Yao, and X. Huang, Effect of Saccharin on the Process and Properties of Nickel Electrodeposition from Sulfate Electrolyte, *International Journal of Metallurgical & Materials Engineering*, Apr. 2016, **2016**. Publisher: Graphy Publications.

[33] Y. Nakamura, N. Kaneko, M. Watanabe, and H. Nezu, Effects of saccharin and aliphatic alcohols on the electrocrystallization of nickel, *Journal of applied electrochemistry*, 1994, **24**, 227–232.

[34] S.-M. Lin, The Effect of Additives on the Internal Stress Of Nickel Deposits from Watts Baths, 1991.

[35] A. M. El-Sherik, J. Shirokoff, and U. Erb, Stress measurements in nanocrystalline Ni electrodeposits, *Journal of Alloys and Compounds*, Mar. 2005, **389**, 140–143.

[36] R. Hoffman, Stresses in thin films: The relevance of grain boundaries and impurities, *Thin Solid Films*, 1976, **34**, 185–190.

[37] E. Chason, A kinetic analysis of residual stress evolution in polycrystalline thin films, *Thin Solid Films*, 2012, **526**, 1–14.

[38] A. Monshi, M. R. Foroughi, M. R. Monshi, *et al.*, Modified scherrer equation to estimate more accurately nano-crystallite size using xrd, *World journal of nano science and engineering*, 2012, **2**, 154–160.

[39] A. Ul-Hamid, *A beginners' guide to scanning electron microscopy*, vol. 1. Springer, 2018.

[40] D. K. Pandey, H. L. Kagdada, P. Sanchora, and D. K. Singh, Overview of Raman Spectroscopy: Fundamental to Applications, in *Modern Techniques of Spectroscopy: Basics, Instrumentation, and Applications* (D. K. Singh, M. Pradhan, and A. Materny, eds.), Progress in Optical Science and Photonics, 145–184, Singapore: Springer, 2021.

[41] L. M. Malard, M. A. Pimenta, G. Dresselhaus, and M. S. Dresselhaus, Raman spectroscopy in graphene, *Physics Reports*, Apr. 2009, **473**, 51–87.

[42] I. Calizo, I. Bejenari, M. Rahman, G. Liu, and A. A. Balandin, Ultraviolet Raman microscopy of single and multilayer graphene, *Journal of Applied Physics*, Aug. 2009, **106**, 043509.

[43] P. Kidd, Xrd of gallium nitride and related compounds: strain, composition and layer thickness, *Panalytical: Almelo, Netherlands*, 2009, 119.

[44] S. Chowdhury, M. T. Laugier, and J. Henry, XRD stress analysis of CVD diamond coatings on SiC substrates, *International Journal of Refractory Metals and Hard Materials*, Jan. 2007, **25**, 39–45.

[45] J.-H. Min, K.-H. Li, Y.-H. Kim, *et al.*, Toward Large-Scale Ga2O3 Membranes via Quasi-Van Der Waals Epitaxy on Epitaxial Graphene Layers, *ACS Applied Materials & Interfaces*, Mar. 2021, **13**, 13410–13418. Publisher: American Chemical Society.

[46] X. Han, J. Yu, Z. Li, *et al.*, Remote epitaxy and exfoliation of gan via graphene, *ACS Applied Electronic Materials*, 2022, **4**, 5326–5332.

[47] H.-M. Kwak, J. Kim, J.-S. Lee, *et al.*, 2d-material-assisted gan growth on gan template by mocvd and its exfoliation strategy, *ACS Applied Materials & Interfaces*, 2023, **15**, 59025–59036.

[48] Y. Qu, Y. Xu, B. Cao, Y. Wang, J. Wang, L. Shi, and K. Xu, Long-range orbital hybridization in remote epitaxy: The nucleation mechanism of gan on different substrates via single-layer graphene, *ACS Applied Materials & Interfaces*, 2022, **14**, 2263–2274.

[49] P. Predeep, *Optoelectronics: Materials and Techniques*. BoD – Books on Demand, Sept. 2011. Google-Books-ID: wOqPDwAAQBAJ.

[50] "Easy Transfer: Monolayer Graphene on Polymer Film."

[51] Z. H. Ni, T. Yu, Y. H. Lu, Y. Y. Wang, Y. P. Feng, and Z. X. Shen, Uniaxial strain on graphene: Raman spectroscopy study and band-gap opening, *ACS nano*, 2008, **2**, 2301–2305.

[52] A. Shivayogimath, P. R. Whelan, D. M. Mackenzie, *et al.*, Do-It-Yourself Transfer of Large-Area Graphene Using an Office Laminator and Water, *Chemistry of Materials*, Apr. 2019, **31**, 2328–2336. Publisher: American Chemical Society.

[53] R. Ollier, C. Perez, and V. Alvarez, Effect of relative humidity on the mechanical properties of micro and nanocomposites of polyvinyl alcohol, *Procedia Materials Science*, 2012, **1**, 499–505.

[54] O. Sadiku-Agboola, E. Sadiku, O. Ojo, O. Akanji, and O. Biotidara, Influence of operation parameters on metal deposition in bright nickel-plating process, *Portugaliae Electrochimica Acta*, 2011, **29**, 91–100.

[55] R. Downs, K. Bartelmehs, G. Gibbs, and M. Boisen, Interactive software for calculating and displaying x-ray or neutron powder diffractometer patterns of crystalline materials, *American Mineralogist*, 1993, **78**, 1104–1107.

[56] C. Wu, J. Yu, Y. E, *et al.*, Model for low-temperature growth of gallium nitride, *Crystal Growth & Design*, 2016, **16**, 5023–5029.

[57] A. B. Slimane, A. Najar, R. Elafandy, D. P. San-Román-Alerigi, D. Anjum, T. K. Ng, and B. S. Ooi, On the phenomenon of large photoluminescence red shift in gan nanoparticles, *Nanoscale research letters*, 2013, **8**, 1–6.

[58] H. Zhang, J.-H. Min, T.-H. Chung, *et al.*, Nanostructured gallium nitride membrane at wafer scale for photo (electro) catalytic polluted water remediation, *Advanced Science*, 2023, **10**, 2205612.

GaN membranų formavimas naudojant grafeną

Dominykas Augulis

Santrauka

Lankstūs elektronikos prietaisai jau yra naudojami visame pasaulyje pramonėje, moksle ir medicinoje. Taikant šią naujos kartos elektroniką, sveikatos stebėjimas gali būti atliekamas neinvaziniu arba minimaliai invaziniu būdu naudojant lanksčius jutiklius. Tokius jutiklius galima nešioti kaip akinius, papuošalus, rankinius laikrodžius, tatuiruotes primenančius prietaisus ir tekstilės gaminius. Dar viena šios technologijos taikymo sritis yra robotika, kurioje lankstūs jutikliai leidžia robotams imituoti gyvų organizmų pojūčius. Tačiau ar tai būtų žmonės, ar robotai, šie prietaisai kelia didelį cheminį ir inžinerinį iššūkį. Tai atsitinka dėl to, kad elektroniniai komponentai paprastai yra trapūs ir nelankstūs.

Lankstiems prietaisams gaminti yra pasirenkamos kelios gamybos strategijos: taikyti natūraliai galinčias deformuotis organines medžiagas arba rasti sprendimus, kaip neorganinėms medžiagoms suteikti lankstumo. Vienas pirmųjų lanksčios elektronikos srityje pasiektų proveržių buvo komandos, vadovaujamos *T. Someya*, iš Tokijo universiteto. Komanda pranešė apie lanksčios organinės elektronikos lopinėlį, kuris galėjo būti naudojamas kaip robotų oda [1]. Nors šis inžinerinis proveržis yra svarbus, tam tikriems taikymams reikia medžiagų su didesniu krūvininkų judriu ir fizinėmis savybėmis, kurios nekistų esant nepalankiomis aplinkos sąlygomis. Tad, neorganinė optoelektronika tampa geresnė alternatyva.

Neorganinių medžiagų naudojimas lanksčiai elektronikai kelia daug iššūkių, susijusių su didžiuliu mechaniniu nesuderinamumu tarp neorganinių puslaidininkių ir lanksčių pagrindų. Sprendimas šiai problemai - gaminti plonus sluoksnius, nes plonos plėvelės yra lanksčios, atsižvelgiant į tai, kad kritinis lenkimo spindulys yra didesnis plonoms medžiagoms nei tūrinėms [3]. Šiame darbe būtent ir buvo pademonstruota plonų epitaksinių GaN sluoksnių gamyba naudojant dvimatės medžiagos grafeno tarpsluoksnį.

Dvimatė medžiaga buvo naudota kaip tarpsluoksnis tarp auginimo padėklo ir augančio GaN. Grafenas be laisvų jungčių riboja stiprių cheminių jungčių susidarymą ir įgalina vėlesnį sluoksnio nulupimą. Be to, aukštos kristalinės kokybės medžiagos gali būti auginamos naudojant nuotolinę arba dvimatės medžiagos skylių inicijuotą epitaksiją [5]. Tokių auginimų metu padėklas po grafeno sluoksniu moduliuoja auginamas struktūras. Ankstesni tyrimai parodė šios technologijos naudą vertikaliai sudedamiems mikro šviestukams [6]. Be to, ploni GaN sluoksniai turi perspektyvą robotikos srityje, nes GaN ir jo lydiniai pasižymi piezoelektrinėmis savybėmis, kurios puikiai tinka lytėjimo sensorių gamybai.

Šio tyrimo tikslas buvo nukelti ploną ir lankstų GaN sluoksnį nuo auginimo padėklo su grafenu. Tikslui pasiekti buvo suformuotos užduotys:

- Perkelti grafeną ant auginimo padėklo naudojant įprastą šlapiąjį perkėlimo metodą ir naują metodą - naudojant laminatorių.
- Užauginti GaN per grafeno tarpsluoksnį naudojant MOPVE reaktorių.

- Nusodinti Ni įtempimą sukeliančią dangą ant epitaksinio GaN ir įvertinti įtempimo mąstą.
- Nukelti plonus GaN sluoksnius nuo grafeno ir juos ištirti.

Šiame darbe buvo aprašyta teorija, reikalinga suprasti GaN auginimo pagrindus naudojant grafeną bei polikristalinių dangų įtempimo susidarymus. Tyrime nagrinėjamas grafeno perkėlimas taikant šlapiąjį perkėlimo metodą bei perkėlimą su laminatoriumi. Ant perkelto grafeno užauginti ploni GaN sluoksniai nukelti su Ni įtempimą sukeliančiu sluoksniu. Nukeltų dangų morfologija bei cheminė sudėtis analizuota naudojant SEM, EDX ir katodoliuminescenciją.